



Article

Spatiotemporal Projections of Precipitation in the Lancang–Mekong River Basin Based on CMIP6 Models

Zhouliang Sun ^{1,2} , Yanli Liu ^{2,3,4,5} , Jianyun Zhang ^{1,2,*}, Hua Chen ¹ , Junliang Jin ^{2,3,4}, Cuishan Liu ^{2,3,4}, Guoqing Wang ^{2,3,4} and Liushan Tang ²

¹ State Key Laboratory of Water Resources Engineering and Management, Wuhan University, Wuhan 430072, China; zlsun19@whu.edu.cn (Z.S.); chua@whu.edu.cn (H.C.)

² State Key Laboratory of Hydrology-Water Resources and Hydraulic Engineering, Nanjing Hydraulic Research Institute, Nanjing 210098, China; ylliu@nhri.cn (Y.L.); jljin@nhri.cn (J.J.); csliu@nhri.cn (C.L.); gqwang@nhri.cn (G.W.); lstang@nhri.cn (L.T.)

³ Research Center for Climate Change of Ministry of Water Resources, Nanjing 210029, China

⁴ Yangtze Institute for Conservation and Development, Nanjing 210098, China

⁵ Cooperative Innovation Center for Water Safety and Hydro Science, Hohai University, Nanjing 210098, China

* Correspondence: jyzhang@nhri.cn

Abstract: The Lancang–Mekong River Basin (LMRB) is the largest international river in Southeast Asia, supporting a population of about 70 million people. Precipitation is the main source of water resources in the basin, with significant impacts on ecology, production, and livelihoods in the basin. In this study, future precipitation was projected using the Coupled Model Intercomparison Project Phase 6 (CMIP6) climate models. The initial bias of each model was corrected using the daily bias-correction (DBC) method, and then the models were ensembled using the Bayesian model-averaging (BMA) method. The evaluation, based on metrics such as climatology bias, root-mean-square error (RMSE), mean absolute error (MAE), and correlation coefficient (COR), showed that the ensemble precipitation performs better than the individual models. Precipitation under four future Shared Socioeconomic Pathway scenarios (SSP126, SSP245, SSP370, SSP585) displayed an increasing trend throughout the LMRB. The anomalies in annual precipitation in 2061–2090 under each scenario are 136 mm, 142 mm, 114 mm, and 227 mm, in that order. Precipitation in spring and winter shows a trend of increasing in the northern LMRB and decreasing in the southern LMRB, and precipitation in summer and autumn shows a significant trend of increasing in almost the whole basin (significance level 0.05). Spring precipitation in the Mekong Delta decreases in all scenarios. The ratio of wet-season precipitation to dry-season precipitation shows an increasing trend for all scenarios, indicating that the difference between wet-season precipitation and dry-season precipitation will increase in the future. For daily precipitation, the Lancang River Basin (LRB) is dominated by a 3–5% increase in the number of days with 5–10 mm/d of precipitation and the Mekong River Basin (MRB) by a 3–5% increase in the number of days with 10–20 mm/d of precipitation under four SSP scenarios in 2061–2090. There are important changes in the spatial distribution of future precipitation, with the 2500 mm isohyet expanding outwards in a circular pattern and the center of the 1500 mm isohyet moving westwards; i.e., areas with annual precipitation exceeding 2500 mm and 1500 mm will expand. For dry-season precipitation, the 500 mm isohyet shrinks, mainly in a circular pattern towards the center, while the 300 mm isohyet moves mainly towards the east, indicating that areas of dry-season precipitation below 500 mm and 300 mm will expand. In the future, the LMRB will generally become wetter in the wet season and drier in the dry season.



Citation: Sun, Z.; Liu, Y.; Zhang, J.; Chen, H.; Jin, J.; Liu, C.; Wang, G.; Tang, L. Spatiotemporal Projections of Precipitation in the Lancang–Mekong River Basin Based on CMIP6 Models. *Remote Sens.* **2023**, *15*, 4502. <https://doi.org/10.3390/rs15184502>

Academic Editor: Kenji Nakamura

Received: 16 August 2023

Revised: 7 September 2023

Accepted: 11 September 2023

Published: 13 September 2023



Copyright: © 2023 by the authors. Licensee MDPI, Basel, Switzerland. This article is an open access article distributed under the terms and conditions of the Creative Commons Attribution (CC BY) license (<https://creativecommons.org/licenses/by/4.0/>).

Keywords: climate change; precipitation; spatial characteristic; CMIP6; Lancang–Mekong River basin

1. Introduction

Precipitation is the key hydrological process in the global hydrological cycle, and changes in precipitation have always been of interest to the geosciences [1,2]. Precipitation

is the most important indicator for detecting and diagnosing global change, as well as an important driver of global change [3–5]. Observations show a radical change in global precipitation patterns [6–9], characterized by an increase in annual precipitation and the frequency of extreme precipitation events [10,11]. This makes us aware that global climatic conditions are changing dramatically and that we are and will soon be faced with the enormous challenge of adapting to climate change [12–14]. Precipitation is a sensitive factor in climate change [15,16]; it is often used as an important lens to analyze the severity of climate change and its impacts on security and livability [17,18], water resources [19,20], agricultural and livestock production [21–23], the ecological environment [24,25], renewable energy [26–28], and other things. Studies have shown that climate change is already affecting precipitation patterns in many parts of the world, including typical regions such as the Alps in Europe [29], the Qinghai–Tibet Plateau [30], Australia [31], the Mississippi River Basin in North America [32], the Nile and Congo river basins in Africa [33,34], the Amazon Basin in South America [35], dryland in Central Asia [36,37], the Lancang–Mekong River Basin (LMRB) in Southeast Asia [38], the Yangtze River Basin in China [39,40], and many other typical regions of concern.

The Lancang–Mekong River (LMR) is the most important international river in Southeast Asia, and changes in its precipitation directly affect the ecological conditions and livelihoods of people in the basin [41,42]. It originates on the Tibetan Plateau, known as the water tower of Asia, a region that is significantly affected by climate change [43–47]. It is the mother river of Southeast Asia, known as the “Danube of the East”, and flows through five countries in Southeast Asia: Myanmar, Laos, Cambodia, Thailand, and Vietnam [48]. The LMRB crosses cold, temperate, and tropical zones from north to south, making the climate complex and variable, and is also a region sensitive to climate change [49,50]. The main source of water resources in the LMRB is precipitation, and changes in hydrological conditions have a direct impact on the survival of the populations of the countries in the basin, as well as on irrigated agriculture, hydropower, fisheries, ecology, and other areas [51–55]. Agriculture accounts for up to 90% of all water use in the LMRB [56,57], and there are prominent international water disputes [58,59], and all this irrigation water is essentially from precipitation. Meanwhile, droughts and floods are common in the LMRB [60], so changes in precipitation have a direct impact on water security and international relations in the LMRB [61–63].

Precipitation in the LMRB has changed significantly over the historical period. Irannezhad et al. [38] analyzed precipitation changes in the LMRB from 1952 to 2015 using data from the Global Precipitation Climatology Centre (GPCC) and found that annual precipitation showed a wetter trend in the northeastern part of the basin and a predominantly drier trend in the western part. Irannezhad et al. [64] analyzed the characteristics of extreme precipitation in the LMRB from 1952 to 2015 and found no significant trends in the intensity, frequency, or duration of precipitation at the basin scale, but there was a significant increase in the number of wet days, the number of consecutive wet days, and the intensity and frequency of extreme precipitation at the sub-regional scale. For the LRB, Guo et al. [65] found no trend change in precipitation from 1957 to 2011 at six meteorological stations in the upper LRB. Wang et al. [66] found that there was a general trend of increasing precipitation in the middle and lower LRB from 1960 to 2009, but the trend of precipitation changes in summer and autumn showed obvious spatial differences, decreasing at annual and seasonal scales since 2000–2009. For the MRB, Hapuarachchi et al. [67] found no significant trend in precipitation in the Mekong River Basin (MRB) from 1972 to 2000, based on precipitation observations at 65 stations. Based on CHIRPS (Climate Hazards Group InfraRed Precipitation with Station data), Mondal et al. [68] found that the rice-growing region in the Mekong Delta of Vietnam was in a trend of drought with a significant 30% decrease in precipitation during 2000–2018.

Currently, there are few studies of future precipitation changes in the LMRB based on the Coupled Model Intercomparison Project Phase 6 (CMIP6) models [69], and most previous studies are based on the CMIP5 models. Anh et al. [70] found an increase in

wet-season precipitation and a decrease in dry-season precipitation in the Mekong Delta for 2036–2065 based on five CMIP5 models under RCP4.5 and RCP8.5. Cook et al. [71] found an increase in precipitation in the lower MRB under the RCP4.5 scenario based on five CMIP5 models. Try et al. [72], based on two CMIP5 models, MRI-AGCM3.2H and MRI-AGCM3.2S, projected a 13–30% increase in extreme discharge and a 19–43% increase in flood inundation area in the lower MRB and Mekong Delta during 2075–2099, mainly due to a 6.6–14.2% increase in precipitation. Sun et al. [73] analyzed future changes in the number of days with different precipitation intensities under the RCP6.0 scenario based on five CMIP5 models and found that wet-season precipitation has an increasing trend while dry-season precipitation is dominated by an increase in the near future, an increase in the lower LMRB, and a decrease in the upper and middle LMRB in the mid- and far future. There is spatial and temporal heterogeneity in the frequency of different rainfall intensities, e.g., a decrease in rainless and drizzly days and an increase in the number of heavy rainfall days in the middle LMRB in the wet season. These studies draw our attention to the precipitation changes in the LMRB based on CMIP6 models.

This study aims to provide a comprehensive understanding of future changes in precipitation in the LMRB. Specific objectives include: (1) to understand the inter-annual trend of future precipitation and its spatial distribution characteristics as well as the precipitation climatology at different periods in the future; (2) to analyze the seasonal characteristics of future precipitation, including the seasonal changes of spring, summer, autumn, and winter, and the characteristics of wet and dry seasons; (3) to analyze the structural changes in daily precipitation by comparing changes in the frequency of daily precipitation with different intensities; (4) to study the spatial distribution of future precipitation, including annual precipitation and dry-season precipitation, based on the spatial variations of representative isohyets.

2. Study Area and Data

2.1. Study Area

The LMRB is one of the most important international rivers in Southeast Asia (Figure 1). It rises in the Tibetan Plateau in China and flows through five countries, Myanmar, Laos, Thailand, Cambodia, and Vietnam, before emptying into the South China Sea at Ho Chi Minh City in Vietnam. Located at 94–107°E and 10–34°N, the LMRB has a watershed area of 811,000 km² and a total length of 4880 km, making it the ninth-longest river in the world. The part of the Lancang–Mekong in China is called the Lancang River, with a catchment area of 165,000 km², accounting for about 20% of the total catchment area [56]. This river, known as the Mekong after it leaves China's borders, includes almost all of Laos and most of Cambodia and Thailand. The upper reaches of the mainstream have a large gradient and are rich in hydroelectric resources. The lower reaches are relatively flat and prone to flooding [74]. There are great differences in topography between the upper and lower reaches of the basin [37]. The average elevation of the upper LMRB (above Yunjinghong) is about 3300 m. The headwaters of the LRB in the northern section are located on the Qinghai–Tibet Plateau at an elevation of over 4000 m. The riverbed in the southern LRB has a steep slope and a deep valley. The basin below Yunjinghong is downstream of the LMRB; the overall terrain is gentler than upstream, and the average elevation is about 400 m. The area below Vientiane is mainly flat; most of the area is 0–300 m above sea level, and a few areas in the east can reach 1000 m. The area between Yunjinghong and Vientiane is 500 to 1000 m above sea level, so it plays a transitional role in elevation.

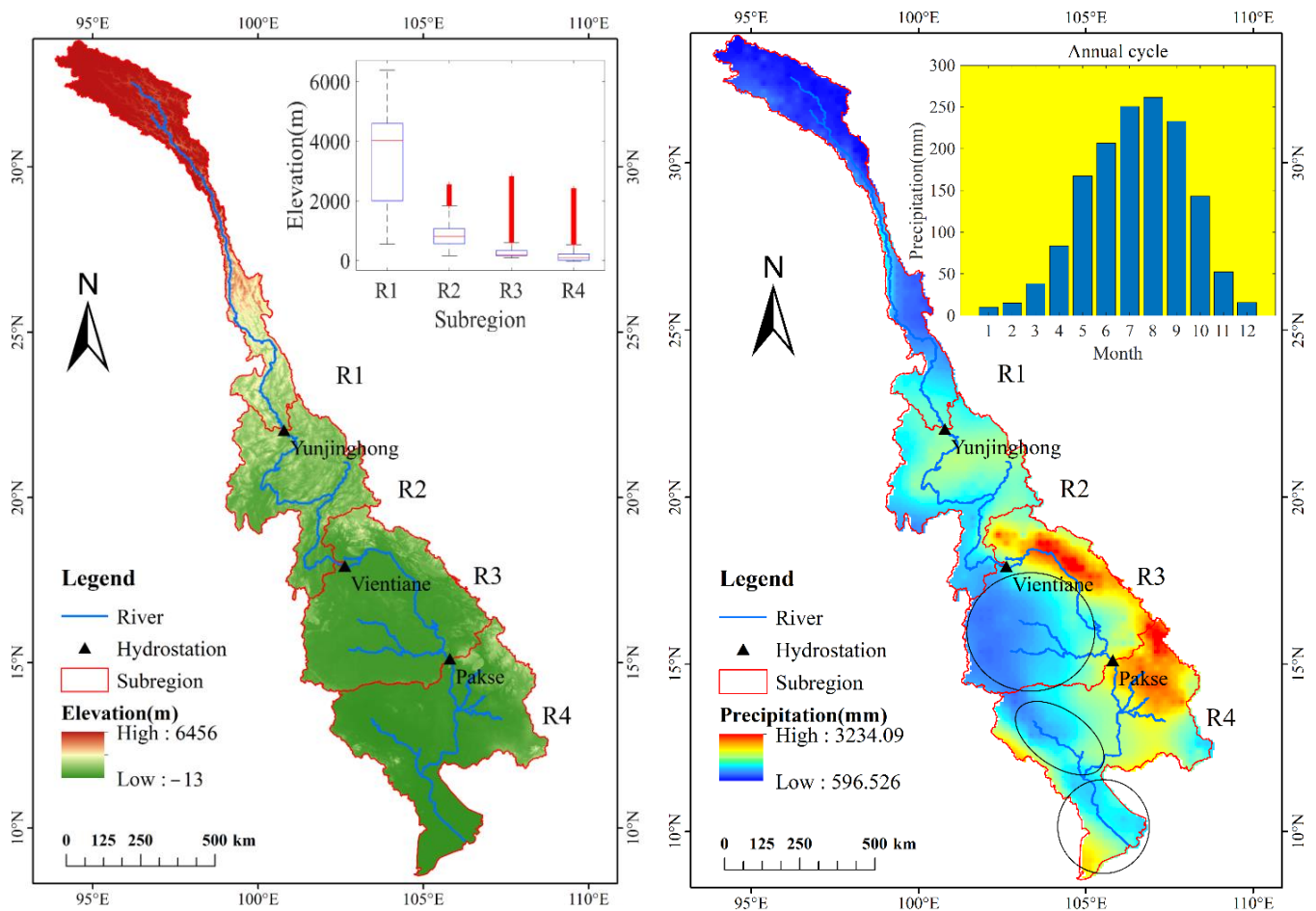


Figure 1. Map of the Lancang–Mekong River Basin and spatial distribution of precipitation. (R1: Lancang River Basin (LCRB); R2: upper Mekong River Basin (UMRB); R3: middle Mekong River Basin (MMRB); R4: lower Mekong River Basin and Mekong Delta (LDMRB); Black circles indicate major rice-growing areas).

The LMR is one of the longest north–south rivers in the world, flowing from north to south through all climate types except a tropical desert climate, with cold areas and low precipitation in the upper reaches, distinct seasonal characteristics of dry and wet seasons in the middle reaches, and hot and humid areas in the lower reaches. The MRB is significantly influenced by different climatic zones and monsoons, with large differences in precipitation and runoff between the dry and wet seasons, with the wet season accounting for more than 85% of annual precipitation [75]. The basin is affected by the southwest monsoon from May to September, with a hot and humid climate. From November to March, it is affected by the northeast monsoon, with a dry climate and low precipitation [76]. The spatial distribution of precipitation and surface water resources in the LMRB is very uneven due to the influence of the monsoon winds from East and South Asia, with annual precipitation in the northern part of the LMRB ranging only from 400 to 800 mm, while annual precipitation in the southern part of Laos and the mountainous fringes of Cambodia and Vietnam can reach up to 3000 mm [77]. The spatial variation in temperature in the basin is also significant, with the average temperature in the upper LRB ranging $-3\sim 3\text{ }^{\circ}\text{C}$, in the middle LRB $12\sim 15\text{ }^{\circ}\text{C}$, and in the lower LRB $15\sim 18\text{ }^{\circ}\text{C}$. Compared with the LRB, the MRB has less spatial variation in temperature, and the highest temperature in the basin is in March–April, with an average temperature of more than $30\text{ }^{\circ}\text{C}$. The lowest temperature is in December, with an average temperature of more than $20\text{ }^{\circ}\text{C}$ [78].

Based on the spatial distribution of topography and climate in the LMRB, the basin can be divided into four regions. The first is the upper Yunjinghong region, which covers most of the LRB and is located in China, with an average multi-year precipitation of about 985 mm. The second is the Yunjinghong–Vientiane interval, or upper MRB, which consists mainly of the northern part of Laos, with an average annual precipitation of 1440 mm. The third is the Vientiane–Pakse interval, or middle MRB, which consists mainly of the eastern part of Thailand and the central and southern parts of Laos, with an average annual precipitation of 1610 mm. There is a rainy zone in the northeast of the region (i.e., the central part of Laos). Finally, the lower Pakse, or lower MRB and delta, includes most of Cambodia, southern Vietnam, and southern Laos, with average annual precipitation of 1770 mm and a rainy zone in the eastern part of the region, roughly within the 3S basin.

2.2. Data Description

We used the output data from the CMIP6 experiment to project future precipitation in the LMRB. In general, there is some uncertainty in climate models and a large bias in the simulation of regional-scale climate [79], especially in some watersheds with complex topography, such as alpine areas like the Tibetan Plateau [80,81]. Several models have been used to improve the reliability of future precipitation projections. Based on the completeness of individual model experiments, we screened 19 models, as shown in Table 1. For each model, we used daily precipitation data from four SSP scenarios (SSP126, SSP245, SSP370 and SSP585). These four scenarios are from the CMIP6 Tier 1 trial (core trial). SSP1, SSP2, SSP3, and SSP5 represent four future socio-economic development pathways, namely sustainability, middle of the road, regional rivalry, and fossil-fueled development, respectively. Specifically, SSP126, SSP245, SSP370, and SSP585 are the low forcing, medium forcing, medium-to-high forcing and high forcing scenarios, respectively, with emissions leading to radiative forcings of 2.6, 4.5, 6.0, and 8.5 Wm^{-2} in 2100, respectively. A bilinear interpolation method was used to interpolate the data from each mode into 0.25° grids, so that the whole basin was divided into 1465 grids.

Table 1. List of CMIP6 GCM models used in this study.

Number	Model (Abbreviation)	Resolution (lon \times lat)	Country or Institution
1	ACCESS-CM2 (ACC)	$1.875^\circ \times 1.25^\circ$	Australia
2	ACCESS-ESM1-5 (ACE)	$1.875^\circ \times 1.25^\circ$	Australia
3	CanESM5 (Can)	$2.8125^\circ \times 2.8125^\circ$	Canada
4	CMCC-ESM2 (CMC)	$1.25^\circ \times 0.9375^\circ$	Italy
5	EC-Earth3 (EC)	$0.703125^\circ \times 0.679245^\circ$	European Union
6	EC-Earth3-Veg (ECV)	$0.703125^\circ \times 0.679245^\circ$	European Union
7	EC-Earth3-Veg-LR (ECL)	$1.125^\circ \times 1.125^\circ$	European Union
8	FGOALS-g3 (FGO)	$2^\circ \times 2.25^\circ$	China
9	GFDL-ESM4 (GFD)	$1.25^\circ \times 1^\circ$	the United States
10	INM-CM4-8 (INM4)	$2^\circ \times 1.5^\circ$	Russia
11	INM-CM5-0 (INM5)	$2^\circ \times 1.5^\circ$	Russia
12	IPSL-CM6A-LR (IPS)	$2.5^\circ \times 1.25^\circ$	France
13	MIROC6 (MIR)	$1.40625^\circ \times 1.40625^\circ$	Japan
14	MPI-ESM1-2-HR (MPH)	$0.9375^\circ \times 0.9375^\circ$	Germany
15	MPI-ESM1-2-LR (MPL)	$1.875^\circ \times 1.875^\circ$	Germany
16	MRI-ESM2-0 (MRI)	$1.125^\circ \times 1.125^\circ$	Japan
17	NorESM2-LM (NoL)	$2.5^\circ \times 1.89474^\circ$	Norway
18	NorESM2-MM (NoM)	$1.25^\circ \times 0.9375^\circ$	Norway
19	TaiESM1 (Tai)	$1.25^\circ \times 0.9375^\circ$	China

To correct the bias of the climate model, we chose the MSWEP gridded precipitation dataset as reference data (<http://www.gloh2o.org/mswep/>, accessed on 30 May 2023). MSWEP is a dataset that merges a wide range of precipitation data products, such as observations, analyzed data, satellite remote-sensing data, etc. [82,83]. A comparative study of 22 global-scale precipitation datasets shows that MSWEP combines the strengths

of several source datasets and generally has the best accuracy [84]. Studies at regional scales such as in the Qinghai–Tibet Plateau [85], the Huaihe River Basin (China) [86], India [87], and the Highlands of Indo-Pak [88] have also shown good performance of MSWEP. In particular, studies by Tang et al. [89,90] and Tian et al. [91] in the LMRB also demonstrate the applicability of MSWEP. We selected MSWEP version V2.2, a dataset that provides 0.1° daily precipitation globally from 1979–2017, with output on a 0.25° grid consistent with the climate model using a bilinear interpolation method.

3. Methodology

3.1. Bias Correction

For climate model bias, this study takes the approach of first correcting the bias and then correcting the multi-model ensemble. The bias correction was performed using the daily bias-correction (DBC) method.

The DBC method is a hybrid method that combines daily translation (DT) and local intensity (LOCI) [92,93]. The LOCI is first used to correct precipitation occurrence so that the frequency of precipitation occurrence in the corrected data for the reference period is equal to the frequency in the observed data for each month. The DT method is then used to correct the frequency distributions of precipitation and temperature to obtain the bias-corrected future daily temperature and precipitation. Instead of applying the same factors to daily precipitation and temperature in a given month, it adjusts the difference between observation and simulation of the same quartile in each month as a function of daily precipitation and temperature based on the interquartile differences in the frequency distributions of precipitation and temperature in the observed data. The DT method is calculated using the following formulas:

$$\begin{aligned} P_{adj,d} &= P_{GCM,d} \times (P_{obs,Q} / P_{GCM,ref,Q}) \\ T_{adj,d} &= T_{GCM,d} + (T_{obs,Q} - T_{GCM,ref,Q}) \end{aligned} \quad (1)$$

where P denotes precipitation, T denotes temperature, Q denotes a quantile for a month, d denotes a historical or future date, adj denotes the corrected variable, GCM denotes the variable before correction, ref denotes the simulation, and obs denotes the observations.

For daily precipitation data, the precipitation frequency (number of wet days) was first corrected using the LOCI approach. For each month, a daily precipitation threshold must be determined; days with daily precipitation greater than this threshold are referred to as wet days so that the simulated frequency of wet days during the historical period is the same as the observed one. The DT method is then applied to correct for the quantile of daily precipitation on wet days. The precipitation thresholds are calculated separately on a monthly basis, taking into account seasonal differences in precipitation. First, the observed frequency of wet days (F_{obs}), which is the ratio of the number of wet days to the total number of days in the month, is calculated according to the observed daily precipitation data for a given month (e.g., January). The simulated daily precipitation for that month is then arranged in reverse order. If the proportion of daily precipitation that is not less than a certain number in the sequence is F_{obs} , this number is the daily precipitation threshold for the month. When the DT method is used to correct the daily precipitation, only the daily precipitation exceeding the threshold is corrected.

Bayesian model averaging (BMA) is a statistical post-processing method based on Bayesian theory that takes into account the uncertainty of the model itself [94,95]. It can organically combine forecasts from different sources and maximize the use of each member model's forecast. The essence of BMA is to compute the posterior distribution of the observation by weighted-averaging the conditional probability distribution of the observation and each member model.

Assuming that P denotes the BMA forecast and D denotes the observed data, $f = [f_1, f_2, \dots, f_K]$ denotes the ensemble of K member model forecasts. The probabilistic forecast formula for the BMA is as follows:

$$p(P|D) = \sum_{k=1}^K p(f_k|D) \cdot p_k(P|f_k, D) \quad (2)$$

where $p(f_k|D)$ is the posterior probability of the k th member model f_k given the observed data D ; in fact, $p(f_k|D)$ is also the weight w_k of BMA, and $p_k(P|f_k, D)$ denotes the posterior distribution of the forecast P given the member model f_k and the data D .

The average BMA forecast is the weighted average of the member model forecasts. If both the member model forecast and the measured data are normally distributed, then the average forecast of the BMA is as follows:

$$E(P|D) = \sum_{k=1}^K p(f_k|D) \cdot E[g(P|f_k, \sigma_k^2)] = \sum_{k=1}^K w_k f_k \quad (3)$$

where w_k and σ_k^2 are the parameters to be calculated; they are usually written as $\theta = \{w_k, \sigma_k^2, k = 1, 2, \dots, K\}$, then the logarithmic form of the likelihood function concerning θ can be expressed as:

$$l(\theta) = \log(p(P|D)) = \log\left(\sum_{k=1}^K w_k \cdot g(P|f_k, \sigma_k^2)\right) \quad (4)$$

where $g(P|f_k, \sigma_k^2)$ denotes a normal distribution with mean f_k and variance σ_k^2 .

It is difficult to find the analytical solution of θ from Equation (3), while the EM algorithm (expectation maximization) can be used with repeated iterations of both the expectation and maximization steps until convergence. A large likelihood value is obtained by EM, which leads to a numerical solution for $\theta = \{w_k, \sigma_k^2\}$, $k = 1, 2, \dots, K$. In the EM, the hidden variable $z_{t,k}$ will be used to compute the BMA weights. Prior to the application of the EM algorithm, the observed and forecast data were generally normalized using the Box–Cox function. The application of the EM algorithm to the calculation of the BMA parameters can be seen in particular in [96,97].

3.2. Trend Analysis

In this study, three methods were used to quantitatively characterize future trends in precipitation: the Mann–Kendall (MK) trend analysis method, linear trend coefficients, and annual mean anomalies.

The MK is an acausal statistical method used to detect trends in time series [98,99], and recommended by the World Meteorological Organization for trend analysis [100,101]. The method assumes that the original data series are random and independent of each other. For all results, the significance of trends is tested at the 5% level. The MK method determines whether Z reaches the threshold corresponding to the significance level at a given significance level by constructing a statistic Z that obeys a normal distribution. The calculation method is:

$$Z = \begin{cases} (S - 1) / \sqrt{\text{Var}(S)} & S > 0 \\ 0 & S = 0 \\ (S + 1) / \sqrt{\text{Var}(S)} & S < 0 \end{cases} \quad (5)$$

$$\text{Var}(S) = n(n - 1)(2n + 5) / 18 \quad (6)$$

$$S = \sum_{k=1}^{n-1} \sum_{j=k+1}^n \text{sgn}(x_j - x_k) \quad (7)$$

$$\text{sgn}(x) = \begin{cases} 1 & x > 0 \\ 0 & x = 0 \\ -1 & x < 0 \end{cases} \quad (8)$$

where n is the sequence length and S is a statistic. At the 0.05 level of significance, if Z is greater than 1.96 it indicates a significant increasing trend and if Z is less than -1.96 it indicates a significant decreasing trend.

The linear trend coefficients are derived from the slope k of a single linear fit based on the least-squares method, using the mathematical model of:

$$y = kx + b \quad (9)$$

where y is the precipitation variable, x is the time variable, k is the linear trend coefficient, and b is a parameter. The parameter k can be used to indicate a linear trend over time, with an increasing trend when k is positive, and a greater absolute value of k results in a greater trend of change.

For future climate change, in addition to long-term-trend changes, we are also concerned with the mean climate change over a given period. We use the anomaly D in a period to represent this trend of change in the mean climate:

$$D = P_{t0} - P_{t1} \quad (10)$$

where $t0$ is the historical base period, $t1$ is a given period in the future, P_{t0} is the multi-year average of the precipitation index P in the base period, and P_{t1} is the multi-year average of the precipitation index P in the future period.

3.3. Evaluation Metrics for Performance

We have selected some commonly used metrics to evaluate the accuracy of precipitation simulations, including *RMSE* (root-mean-square error), *MAE* (mean absolute error), *COR* (correlation coefficient), and *MS* (model spread). The *RMSE* reflects the simulation accuracy of the precipitation process:

$$RMSE = \sqrt{\frac{1}{n} \sum_{t=1}^n (X_{o,t} - X_{s,t})^2} \quad (11)$$

where n is the sequence length, $X_{o,t}$ is the observation, and $X_{s,t}$ is the simulation. The lower the *RMSE*, the better.

MAE reflects the precision of the total deviation:

$$MAE = \frac{1}{n} \sum_{t=1}^n |X_{o,t} - X_{s,t}| \quad (12)$$

where the meaning of each variable is the same as before, and the closer the *MAE* is to 0 the better the simulation accuracy.

COR reflects the consistency of precipitation variables over time:

$$COR = \frac{\sum_{t=1}^n (X_{o,t} - \overline{X_o})(X_{s,t} - \overline{X_s})}{\sqrt{\sum_{t=1}^n (X_{o,t} - \overline{X_o})^2} \times \sqrt{\sum_{t=1}^n (X_{s,t} - \overline{X_s})^2}} \quad (13)$$

where $\overline{X_o}$ denotes the mean of the observed series and $\overline{X_s}$ denotes the mean of the simulated series. The other variables have the same meaning as before. The closer the *COR* is to 1, the more consistent the temporal change is across models.

MS is used to reflect the closeness of the models:

$$MS = \sqrt{\frac{1}{N} \sum_{i=1}^N (X_{s,t,i} - \overline{X_{s,t}})^2} \quad (14)$$

where N is the number of models, $X_{s,t,i}$ is the simulated value for the i th model, and $\overline{X_{s,t}}$ is the mean of the simulated values for each model.

4. Results

4.1. Evaluation of Simulation Deviation

To understand the ability of each climate model to simulate precipitation in the LMRB, the simulation bias of each model for annual mean precipitation over the historical period was first analyzed, as shown in Figure 2. The bias of each model is very pronounced, up to 1500 mm for both overestimation and underestimation, which is in general agreement with the model assessment of Pimonsree et al. using the GPCC reference data [102]. Spatially, overestimation occurs mainly in the upper LMRB; i.e., in the areas with less annual precipitation, such as ACC, ACE, Can, CMC, GFD, INM4, INM5, MIR, NoL, and Tai, the models overestimate the middle and lower part of the R1 region by more than 1000 mm. Underestimation occurs in the lower LMRB in the areas with more annual precipitation, such as ACC, ACE, Can, CMC, ECL, FGO, GFD, IPS, MIR, MPH, MPL, MRI, NoL, NoM, and Tai, where the models underestimated the R3 region and part of the R4 region by more than 1000 mm, which mainly corresponded better with the areas with more than 2500 mm annual precipitation (Figure 1). Except for two models, INM4 and INM5, the bias of the annual precipitation simulation for the R2 region is relatively small, and the overestimation or underestimation is generally within 500 mm.

The DBC method was used to correct the bias of each model. The statistical results of the bias distribution for each model and the multi-model ensemble after correction are shown in Figure 3. Overall, the number of grids with an annual precipitation simulation bias (including overestimation and underestimation) higher than 600 mm is significantly reduced after correction. Comparing the models, the corrected Can, INM4, and INM5 models have more grids with a bias higher than 600 mm, while most of the other models have a bias within 600 mm. To further reduce the simulation bias, the BMA method was used to ensemble the simulation of each model. After the ensemble, the annual precipitation simulation bias of most grids is within 40 mm, and only a few grids have a bias of around 100 mm. From a spatial perspective, there is some overestimation in the middle and lower parts of the R1 region and the central part of the R4 region (Tonle Sap Lake Basin), with an overestimation of around 30–60 mm, and a small amount of underestimation in the eastern parts of the R3 and R4 regions, with an underestimation around 60–100 mm. Although there is still some bias, it is very low compared with the initial bias of the model, and most grids have relative biases of less than 5%.

Figure 4 shows the evaluation of the simulation accuracy of daily precipitation for each model and MME after bias correction. The RMSE is 8–15 mm for most grids of each model on the daily scale and 6–10 mm for the MME. The RMSE is 70–180 mm for most grids of each model on the monthly scale and 50–70 mm for the MME. The MAE is 4–7 mm for most grids of each model on the daily scale and 3–6 mm for the MME. The MAE is 50–120 mm for most grids of each model and 30–50 mm for MME. On the daily scale, the COR of most grids of each model is 0.15–0.25, and the COR of MME is 0.3–0.35, which is still small but significantly improved compared with each model. On the monthly scale, the COR of most grids of each model is 0.55–0.8, and the COR of MME is 0.8–0.9.

Comparing Figures 3 and 4, the precipitation simulation accuracies after correction and ensemble are better, with the total annual precipitation simulation bias within 5% in most regions, and the intra-annual variation in precipitation can be better simulated; i.e., the bias-processing procedures based on DBC and BMA have achieved good performance. For the prediction of future periods, the same bias procedure is used as for the historical periods; i.e., the DBC method is used to correct the bias, and then the BMA method is applied to ensemble-average the projection of each model to obtain the future precipitation projection under four SSP scenarios.

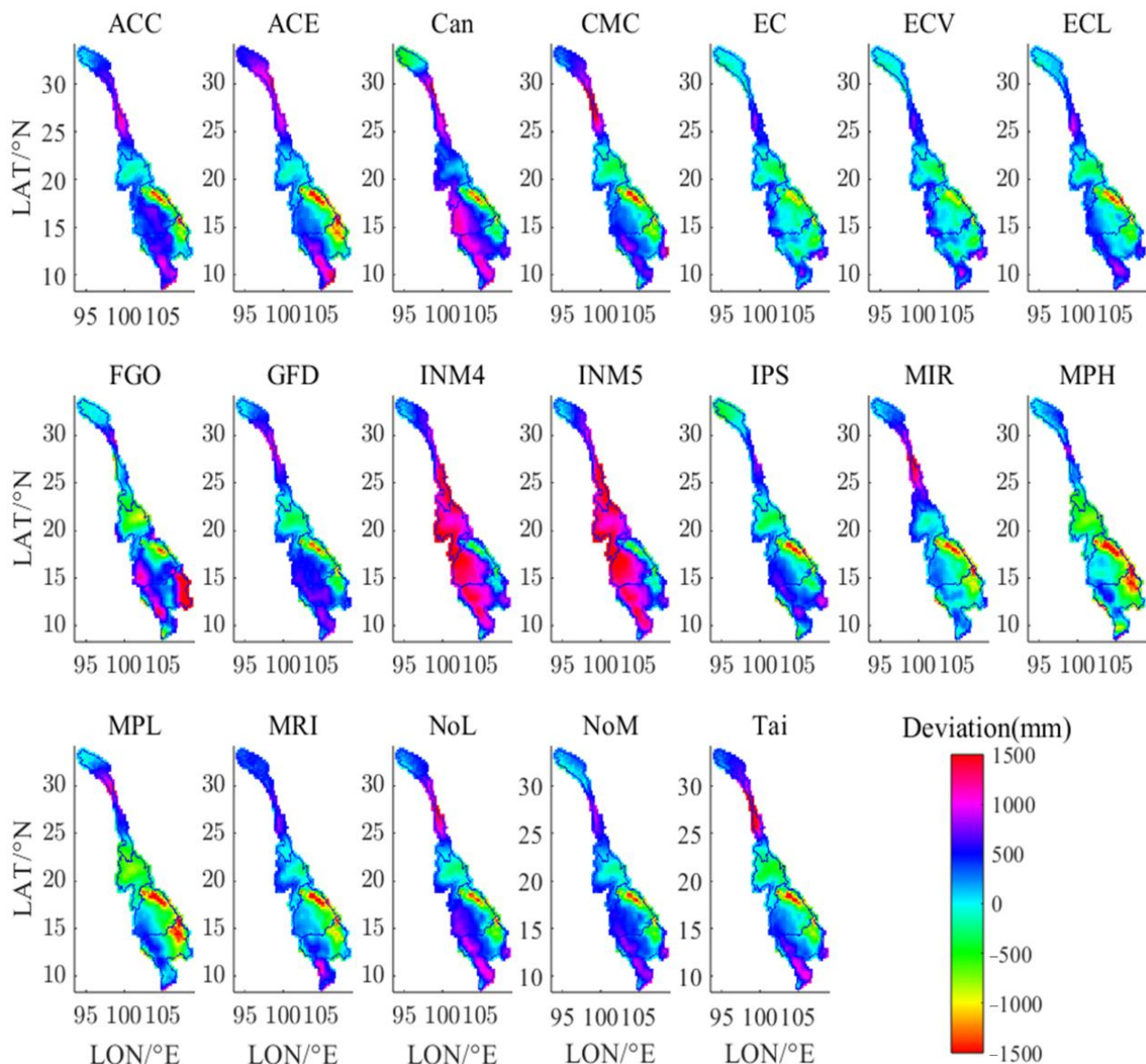


Figure 2. Spatial distribution of initial simulating bias of historical precipitation for each model.

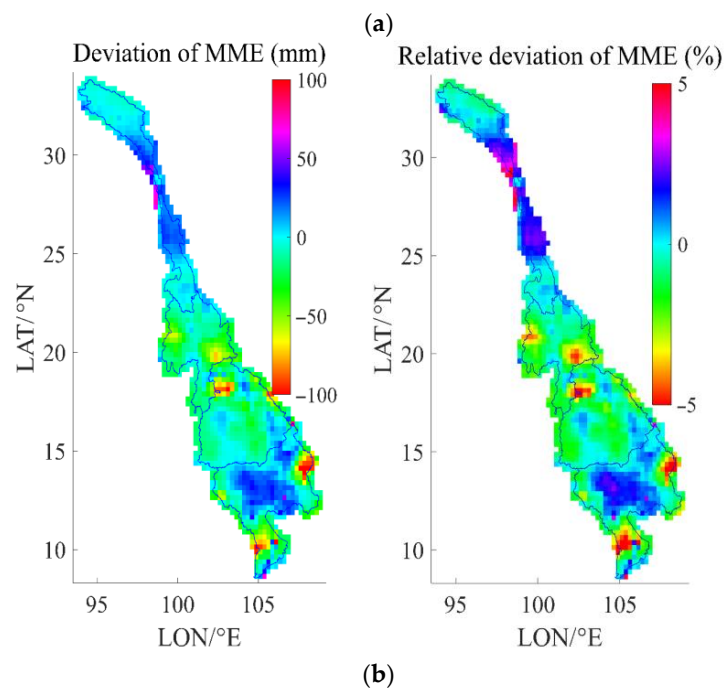
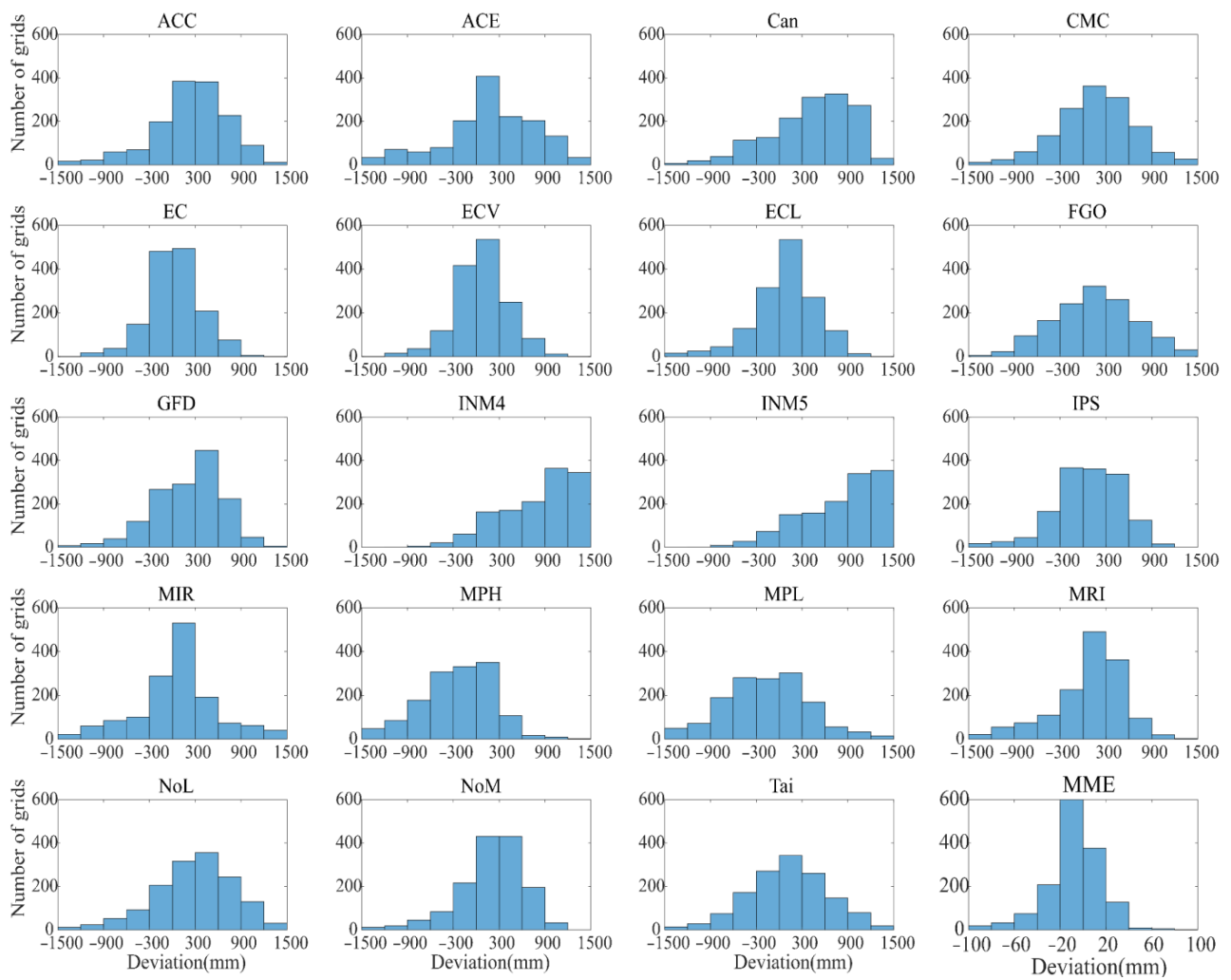


Figure 3. The deviations of each model after correction and multi-model ensemble (MME). (a) Deviation statistics of the corrected model and MME. (b) Spatial distribution of the deviation of the multi-model ensemble.

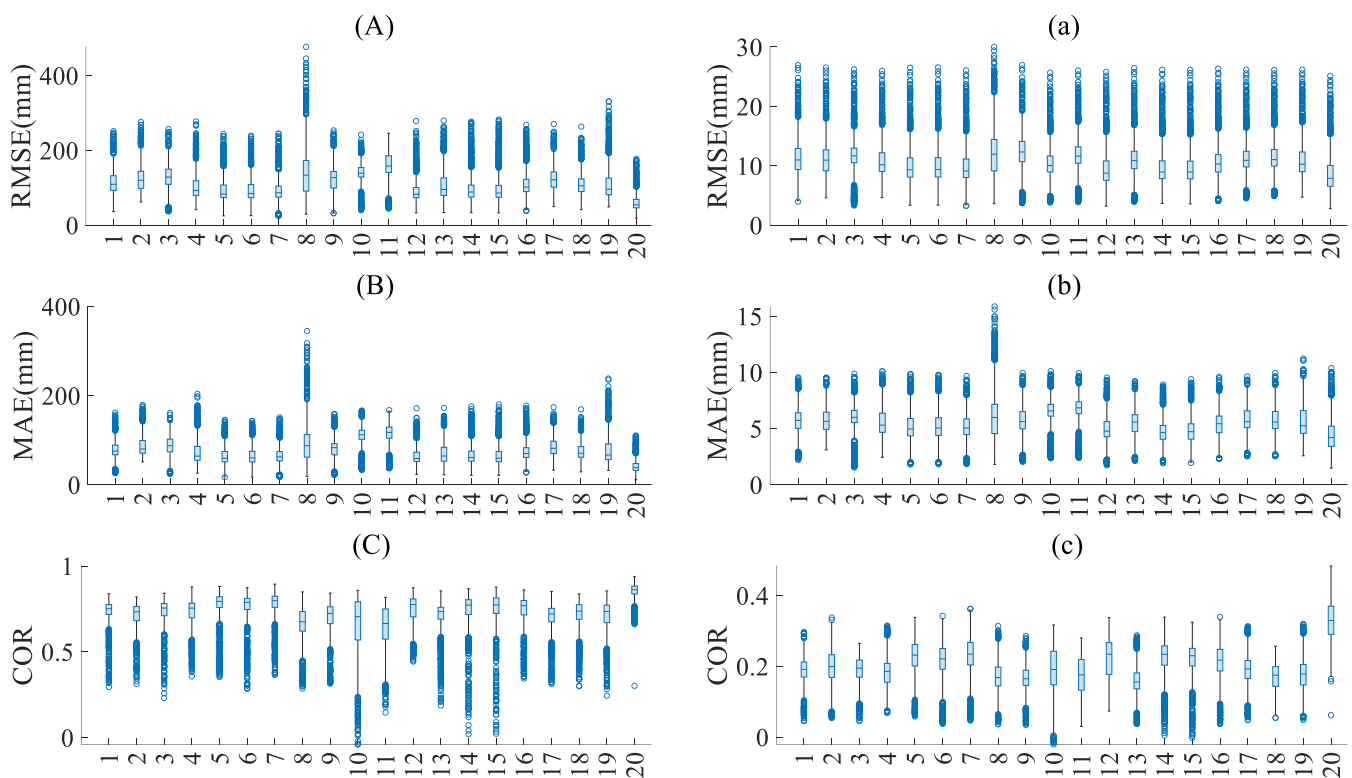


Figure 4. Evaluation of the precipitation simulation accuracy of each model and the multi-model ensemble. (A–C): monthly; (a–c): daily. 1–19 on the X-axis represent the 19 models in Table 1, and 20 represents the MME.

4.2. Trends in Future Precipitation

Figure 5 shows the future annual precipitation trends for each SSP scenario. Precipitation will increase in the future in the whole basin and in each region. The rates of increase in annual precipitation (k in Figure 5) for the whole basin under each SSP scenario are 180 mm/100 a, 240 mm/100 a, 270 mm/100 a, and 510 mm/100 a. Spatially, under SSP126, UMRB precipitation increases at the fastest rate (220 mm/100 a) and LCRB precipitation at the slowest rate (150 mm/100 a); under SSP245, LDMRB precipitation increases at the fastest rate (270 mm/100 a) and LCRB precipitation at the slowest rate (210 mm/100 a); for SSP370, UMRB, LCRB, and LDMRB precipitation increase the fastest (at 300 mm/100 a, 290 mm/100 a, and 290 mm/100 a, respectively) and MMRB precipitation increases the slowest (at 190 mm/100 a); for SSP585, LDMRB precipitation increases the fastest (at 610 mm/100 a) and MMRB and LCRB precipitation increase the slowest (at 440 mm/100 a and 450 mm/100 a, respectively).

Considering the spatial variation in precipitation in the LMRB, the spatial distribution of the rate of increase in annual precipitation is shown in Figure 6. Under SSP126, SSP245, and SSP370, most regions have relatively low rates of increase (approximately no more than 200 mm/100 a), and a few regions have rates of increase exceeding 500 mm/100 a, which, when compared with Figure 1, can be seen to be in the region of higher annual precipitation in the historical period. Under SSP585, the regions with rates of increase greater than 500 mm/100 a increase significantly and completely cover the regions with annual precipitation greater than 2500 mm. This suggests that annual precipitation will increase in all parts of the basin in the future, with regions with higher annual precipitation in previous years increasing at a higher rate.

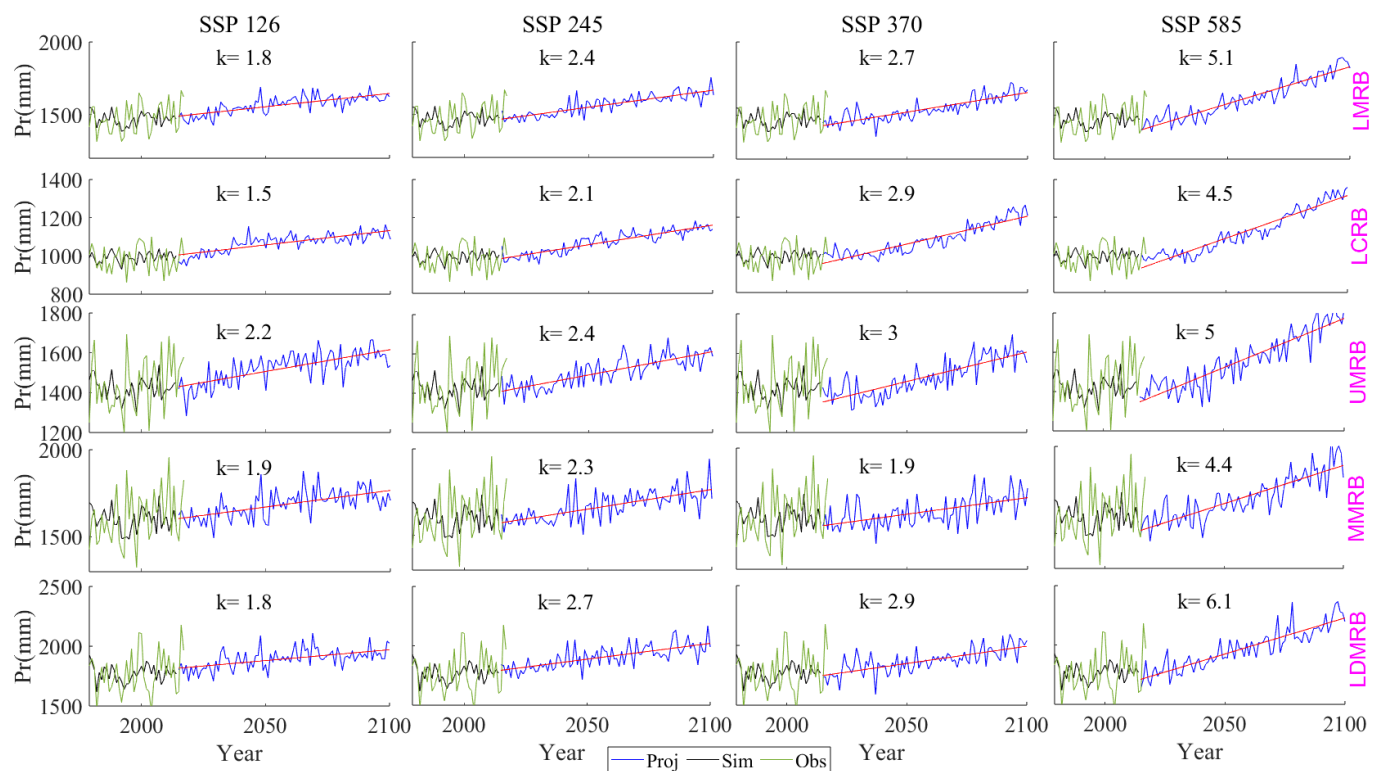


Figure 5. Long-term trends in annual precipitation under different SSP scenarios at different spatial scales in the future (k is a linear trend coefficient).

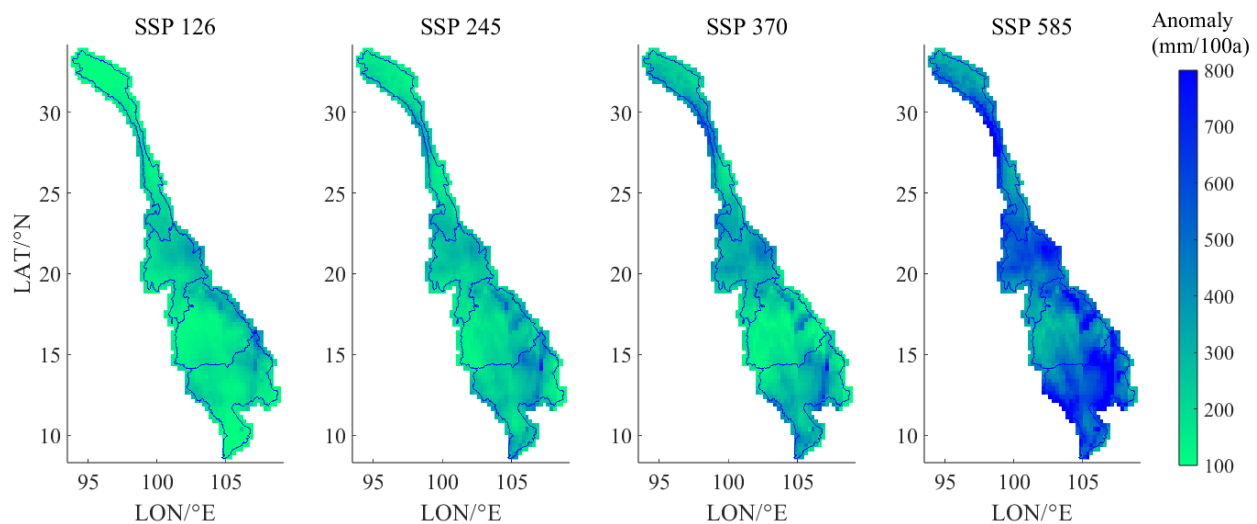


Figure 6. Spatial distribution of the future rate of increase in annual precipitation (mm/100 a, 100 times the k in Figure 5).

To understand the precipitation changes in different periods, two periods were selected in this study; the near future is 2031–2060 and the far future is 2061–2090. Figure 7 shows the anomalies in regional annual average precipitation for the two future periods. The precipitation anomaly in the far future is significantly higher than that in the near future. In the near future, the basin-wide precipitation anomalies are 89 mm, 71 mm, 23 mm, and 70 mm for the four SSP scenarios, while the anomalies in the far future are 136 mm, 142 mm, 114 mm, and 227 mm, respectively. For the UMRB and MMRB, the anomaly in the near future is slightly less than 0, indicating a slight decrease in the two sub-regions in the near future, and it can be assumed that there is no significant change in the UMRB or MMRB

compared with the baseline period. Spatially, the LDMRB has a higher anomaly than the other partitions in the four SSP scenarios in the near and far future, while the MMRB has a lower anomaly than the other partitions in the four SSP scenarios. Comparing the four SSP scenarios, the anomaly for each region is largest in the near future under SSP126 and the largest in the far future under SSP585, indicating that the precipitation increase rate under SSP585 is lower in the near future and higher in the far future.

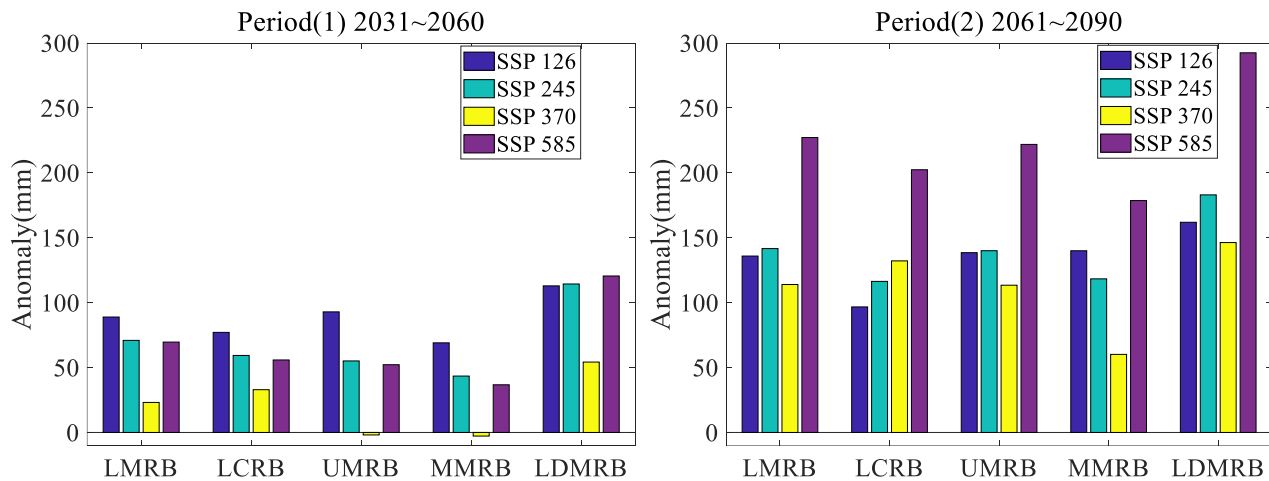


Figure 7. Future annual precipitation anomalies in different regions under four SSP scenarios.

4.3. Annual Cycle of Average Seasonal Precipitation

Figure 8 shows the trend in seasonal precipitation; the trend is expressed using the Z statistic in the MK method. Among the four seasons, there was significant spatial heterogeneity in spring and winter precipitation and a significant increasing trend in summer and autumn precipitation for almost the entire basin.

For spring precipitation, the change in LMRB in all scenarios showed an increasing trend in the north and a decreasing trend in the south. R1 showed a significant increasing trend under all four SSP scenarios. R2 showed a significant increasing trend under SSP126 and SSP585 and a non-significant increasing trend under SSP245 and SSP370. R3 showed an increasing trend over most of the basin under SSP126 and SSP585 and a decreasing trend under SSP245 and SSP370. Most areas of R4 showed an increasing trend under SSP126 and SSP 585, a non-significant decreasing trend in most areas under SSP245, and a significant decreasing trend in most areas under SSP370.

For winter precipitation, under SSP126 there is a significant increasing trend in southern R1 and northern R2 and a non-significant increasing trend in the rest of the basin. Under SSP245, there is a decreasing trend only in the localized area in the southeastern R3 and an increasing trend in all other areas. Under SSP370 and SSP585, there is a significant increasing trend in northern R1, with a predominantly non-significant trend in R4 and a decreasing trend in R2 and R3. Southern R1 shows a significant decreasing trend under SSP370 but no significant trend under 585.

As shown in Figure 1, precipitation in the LMRB mainly occurs during the wet season (May–October), accounting for about 85% of the annual precipitation. Figure 9 shows the changes in monthly precipitation during the wet season in the two future periods. For the basin as a whole, May precipitation will decrease and June to October precipitation will increase in the future compared with the historical base period, with the increase in the far future being higher than that in the near future. At the regional scale, May precipitation will increase only in the LCRM and decrease in all three regions (UMRB, MMRB, and LDMRB) and June–October precipitation will increase mainly in these three regions.

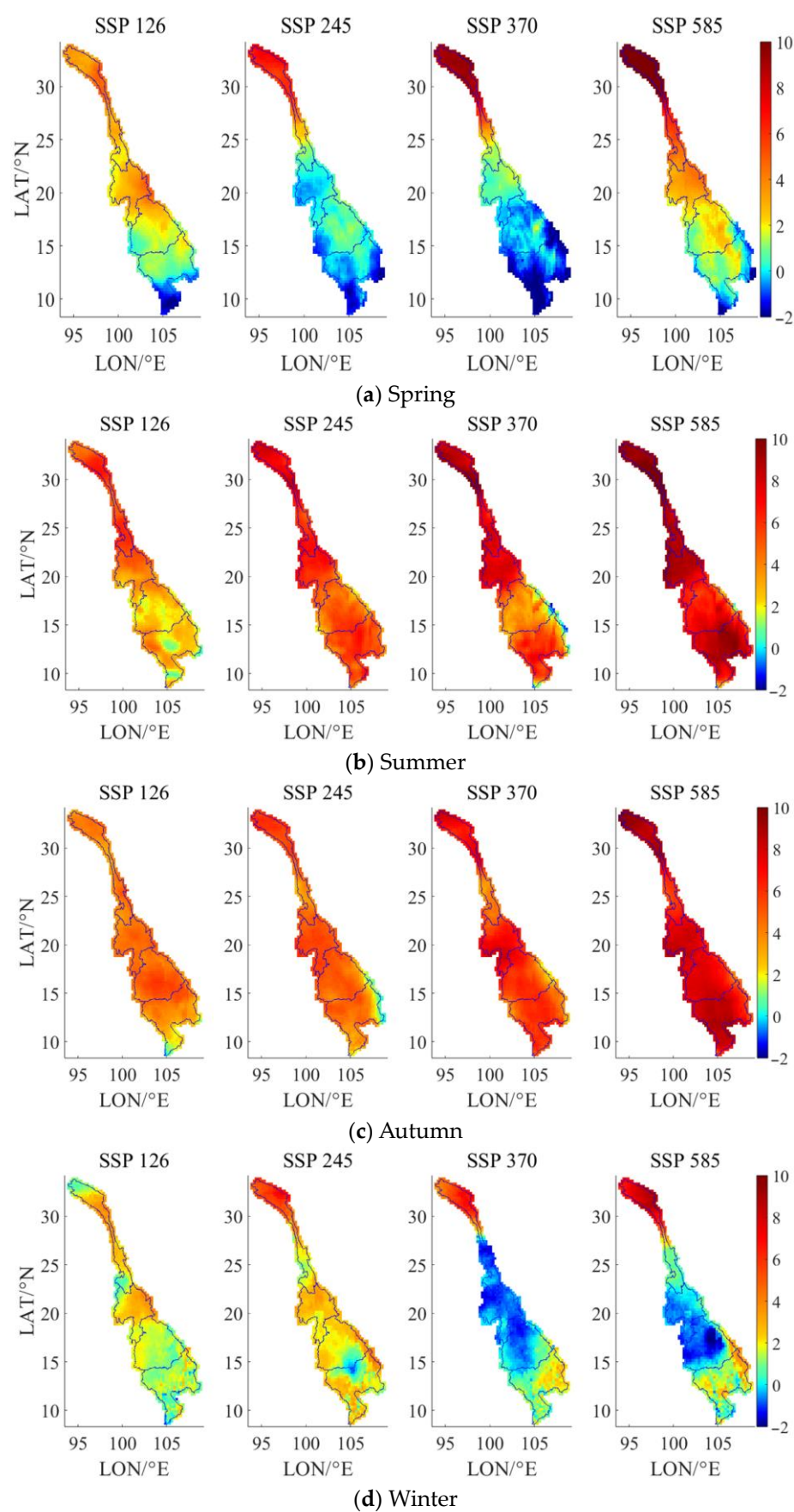


Figure 8. The spatial distribution of the Z statistic of the MK test for future seasonal precipitation variation.

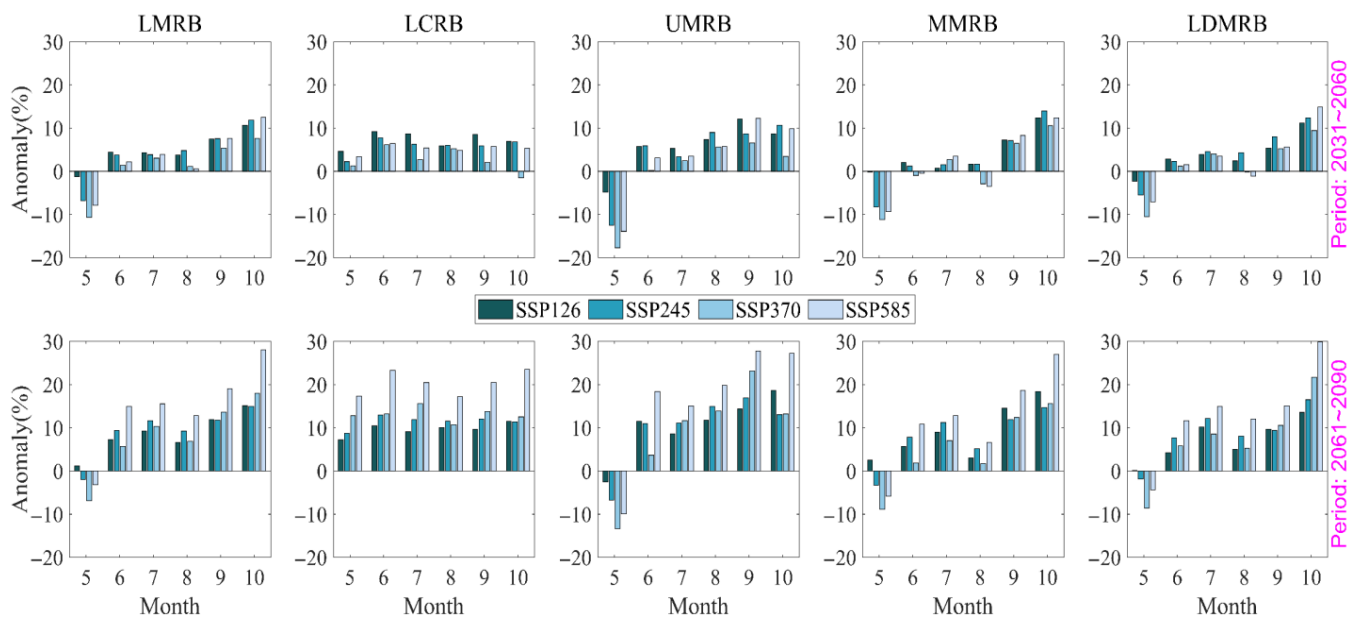


Figure 9. Future changes in monthly precipitation in the wet season (May–October) in different regions.

It is well known that precipitation in the LMRB varies greatly between the wet and dry seasons. Figure 10 shows the ratio of wet- to dry-season precipitation (R_{wd}) in different regions. The greater the difference in precipitation between the wet and dry seasons, the greater the R_{wd} . From the perspective of the whole basin, the R_{wd} shows an increasing trend under all future scenarios, of which the trend is highest under SSP370, indicating that the difference in precipitation between the wet and dry seasons will increase in the future.

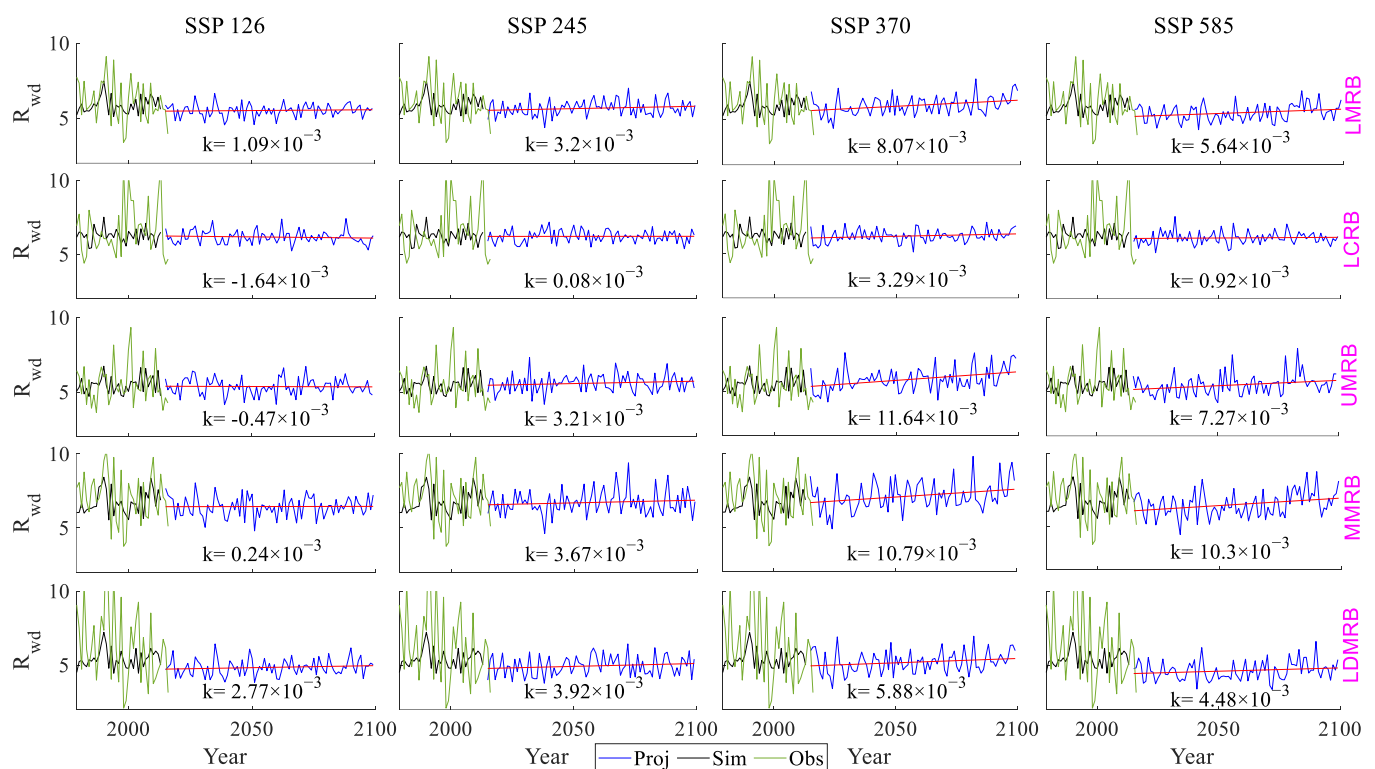


Figure 10. Future changes in the regional ratio of wet- to dry-season precipitation (R_{wd}).

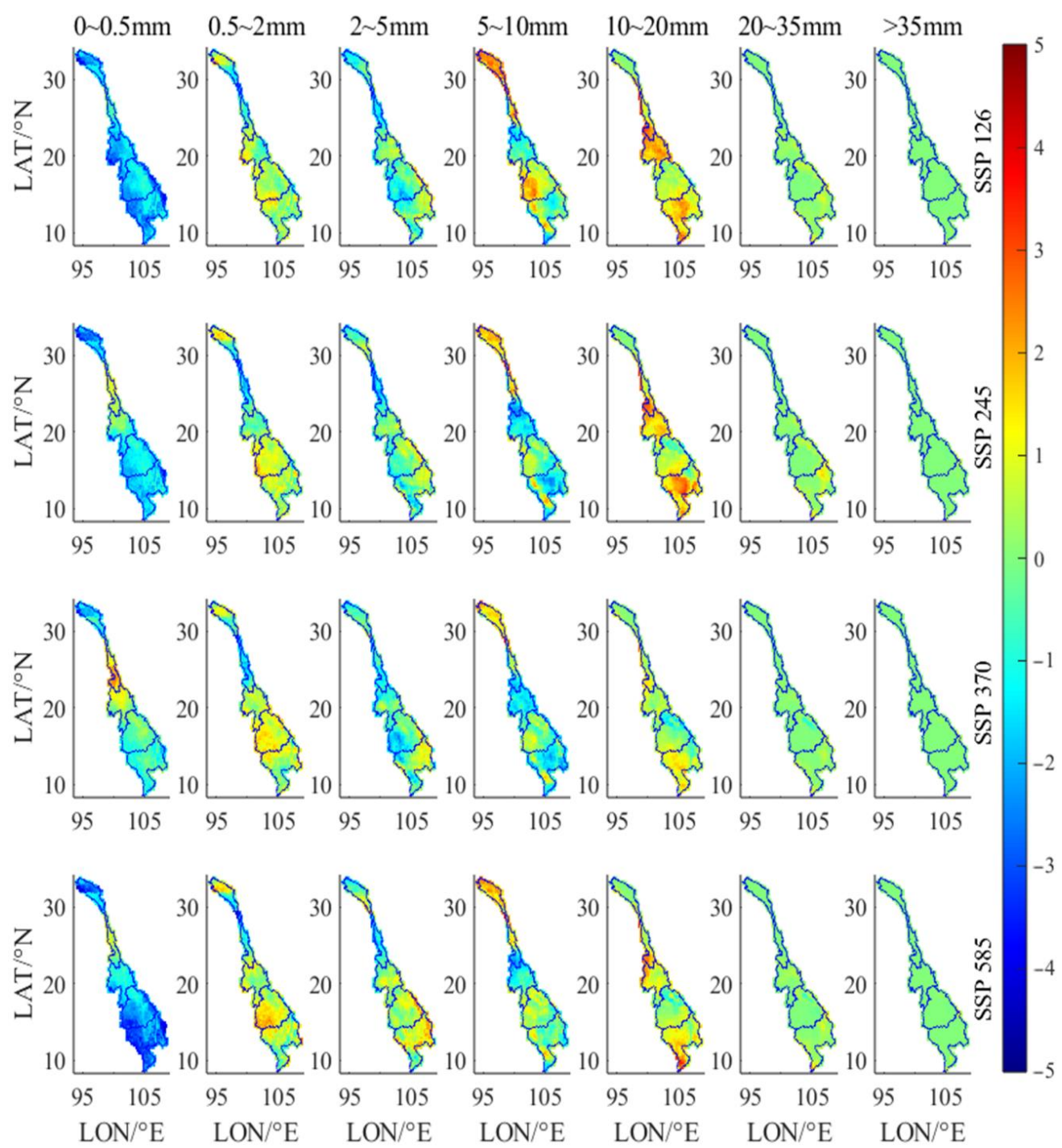
At the regional scale, R_{wd} in R1 shows a decreasing trend under SSP126, i.e., a decrease in the precipitation difference between the wet and dry seasons, a slightly increasing trend under SSP245 and SSP585, and an increasing trend under SSP370. R_{wd} in R2 and R3 show no significant change under SSP126 and an increase under SSP245, SSP370, and SSP585. R_{wd} in R4 has an increasing trend under all scenarios. In general, R_{wd} in the upper LMRB has a decreasing trend or a weak increasing trend, while the middle and lower LMRB show a stronger increasing trend. Among all the regions, the increasing trend for R_{wd} is the highest under SSP370; i.e., the difference in precipitation between the wet season and the dry season will increase the most in the future.

4.4. Changes in Daily Precipitation Composition

Flooding is common in the LMRB, especially downstream [103,104]. In general, flooding in the MRB is caused by heavy rainfall, and an increase in the number of days with heavy rainfall during the wet season will directly lead to an increase in the risk of flooding and damage [74,105]. Changes in precipitation intensity have important implications for people's lives, especially in the LMRB, which is highly vulnerable to floods and droughts [106]. To this end, we counted the changes in the number of days with different precipitation intensities under different scenarios. Based on the distribution of daily precipitation intensity in the LMRB, we classified daily precipitation into seven types, namely 0–0.5 mm/d, 0.5–2 mm/d, 2–5 mm/d, 5–10 mm/d, 10–20 mm/d, 20–35 mm/d, and >35 mm/d [107].

Figure 11 shows the changes in the number of days with seven categories of precipitation. The number of days with a daily precipitation of 0–0.5 mm/d is mainly reduced in most parts of the LMRB under all scenarios, and in the lower LMRB (R3 and R4) is significantly reduced under SSP585 in the near future and SSP126 in the far future. The number of days with daily precipitation of 0.5–2 mm/d increases by 0–2% in most parts of the LMRB in both the near and far futures. The number of days with daily precipitation of 2–5 mm/d varies (increases or decreases) within 1% in the near future and may decrease by 3% in the far future in some areas of the LRB, Tonle Sap Lake Basin, and Mekong Delta. The number of days with daily precipitation of 5–10 mm/d will increase by 1–2% in the LRB in the near future, increase by more than 5% in the far future, decrease in the eastern MRB, and increase in the western MRB. The number of days with daily precipitation of 10–20 mm/d will increase by 1–2% in most areas in the near future, by 2–4% in most areas in the far future, and by more than 5% in some areas. The number of days with daily precipitation of 20–35 mm/d is almost unchanged in the whole basin in the near future and increases by more than 3% in some areas of R3 and R4 in the far future. The number of days with daily precipitation of more than 35 mm/d is almost unchanged in the whole basin in the near and far future.

Based on the above changes, changes in the compositional structure of future daily precipitation occur mainly in the far future. The decrease in the number of days with daily precipitation of 0–0.5 mm/d indicates an increase in the number of wet days. In the far future, the LRB is dominated by a 3–5% increase in the number of days with 5–10 mm/d of precipitation; the MRB is dominated by a 3–5% increase in the number of days with 10–20 mm/d of precipitation. Precipitation of 10–25 mm/d is usually referred to as moderate precipitation, while precipitation above 25 mm/d becomes heavy precipitation [108]. The continuous occurrence of these rainy days is also usually one of the factors contributing to flooding. The MRB is a flood-prone basin, and an increase in the number of days with moderate and heavy precipitation may lead to an increase in the probability of continuous rainy days, which could lead to an increased risk of flooding [109].



(a) Near future

Figure 11. Cont.

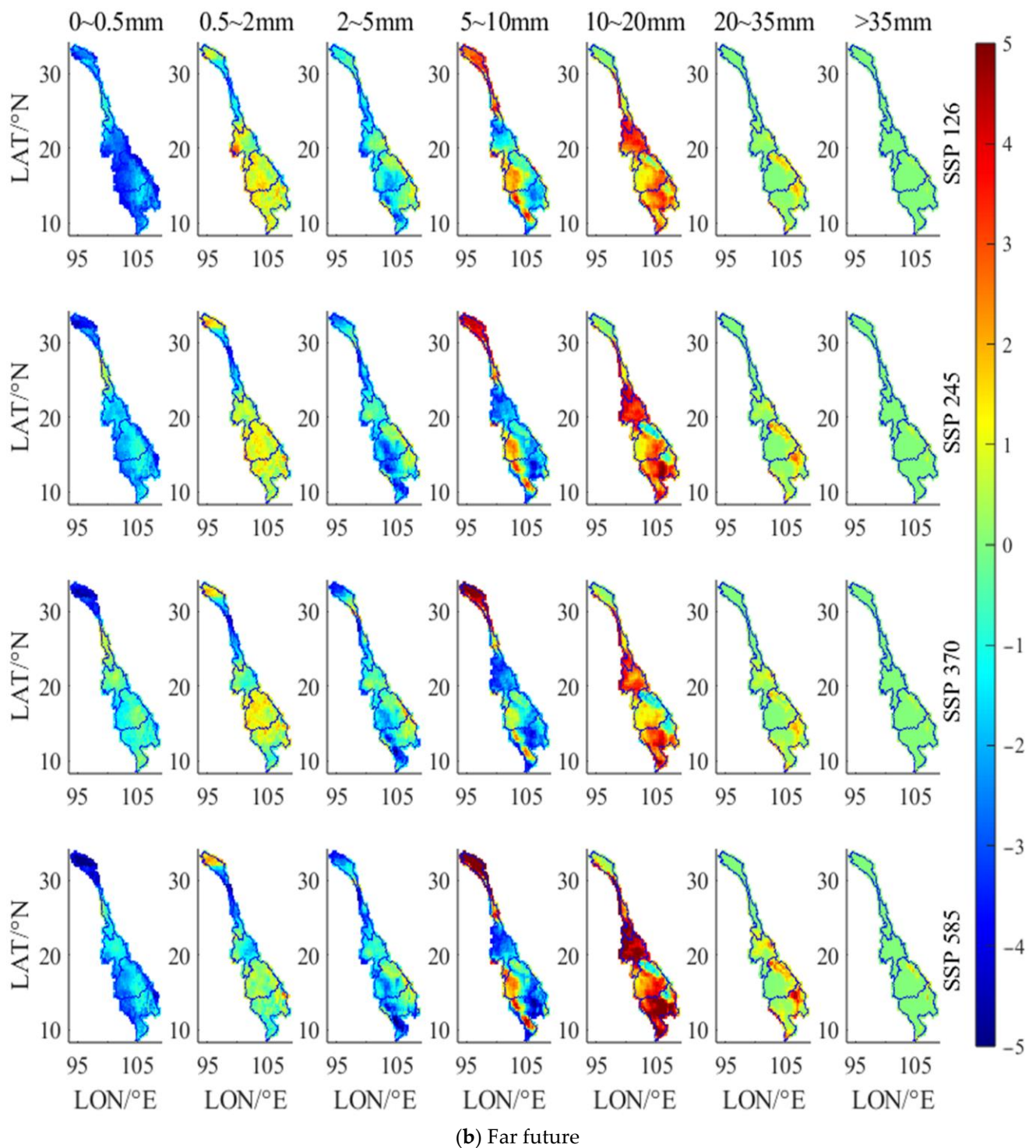


Figure 11. Percentages of anomalies in the number of days with different types of daily precipitation.

4.5. Changes in the Spatial Distribution Characteristics of Future Precipitation

According to the Mekong River Commission report [110], the rice-growing area of the MRB consists of three main areas: most of Thailand, the Tonle Sap floodplain, and the Mekong Delta. It is also an area where annual precipitation is less than 1500 mm (Figure 1). The spatial distribution of precipitation in the LMRB is also very uneven, characterized by low precipitation in the upper reaches, high precipitation in the lower reaches, and low precipitation throughout the basin during the dry season. According to the spatial distribution characteristics of precipitation in the LMRB, two representative

isohyets (precipitation contour) were selected for this study to show the spatial distribution characteristics of precipitation. The first is the 2500 mm isohyet, which mainly includes two rainy areas in the basin, i.e., the central part of Laos (line L1) and the 3S basin at the Laos–Cambodia–Vietnam border (line L2). The second is the 1500 mm isohyet, which is located near the mainstream of the Mekong River and roughly divides the MRB into east and west, with the western part receiving less than 1500 mm of annual precipitation and the eastern part receiving more than 1500 mm of annual precipitation. The spatial distribution of precipitation can be understood by examining the spatial variation of the isohyets.

Figure 12 shows the spatial variability of the annual and dry-season precipitation distribution for the two representative isohyets. We prefer to focus on the simulation of the historical isohyets. The first columns of Figure 12a,b show the historical observed and simulated (based on MME) isohyets. It can be seen that the MME-based isohyets overlap very well with the observed isohyets for both annual and dry-season precipitation. This suggests that the MME can capture the spatial distribution of precipitation well, which gives us confidence in understanding the change in isohyets in future periods. We compared the change in isohyets between the future projection and the simulation for the base period (rather than the observed isohyets) to analyze the spatial variability of future precipitation.

Columns two to five of the first row in Figure 12a show the changes in annual precipitation isohyets in the near future. For the 2500 mm isohyet, line L1 does not change significantly under the four SSP scenarios, and line L2 does not change significantly under SSP370 but shifts slightly to the south (i.e., the area enclosed by the isohyet becomes larger) under SSP126, SSP245, and SSP585. For the 1500 mm isohyet, there is no significant change under SSP370, but the southern part of the isohyet (the boxed part in Figure 12a that lies west of line L2 around the “3S” basin) is shifted westwards under SSP126, SSP245, and SSP585. The above results indicate that there will be no significant change in the spatial distribution of precipitation in the near future under SSP370 and that the area of annual precipitation exceeding 2500 mm will expand under SSP126, SSP245, and SSP585 (i.e., two rainy zones). The westward shift of the southern 1500 mm isohyet suggests that there will be a more significant increase in precipitation in R4 in the near future, resulting in an expansion of the area of annual precipitation above 1500 mm.

Columns two to five of the second row in Figure 12a show the changes in annual precipitation isohyets in the far future. For the 2500 mm isohyet, there is no significant change in line L1 under any of the four SSP scenarios, and line L2 shows a significant shift to the south under all four SSP scenarios. For the 1500 mm isohyet, there is a significant westward shift under all four SSP scenarios, mainly in the northern part (west of R2) and the southern part (west of L2), while there is no significant change in the central part (west of L1, at the ellipse in Figure 12b). Under the four SSP scenarios for the far future, the area of the rainy zone enclosed by line L2 in the 2500 mm isohyet continues to expand as precipitation increases in region R4. The area of annual precipitation above 1500 mm expands westwards from regions R4 and R2, while there is no significant change in region R3. In particular, for the Mekong Delta, there is a slight increase in precipitation in the near future and a significant decrease in the far future, resulting in the gradual contraction of a NW–SE-trending low precipitation zone (annual precipitation below 1500 mm), which shrinks to a smaller ring under SSP585.

Figure 12b shows the variation in the spatial distribution of dry-season precipitation, with the 300 mm and 500 mm isohyets selected as representative isohyets. Like the 2500 mm isohyet for annual precipitation, the 500 mm isohyet consists mainly of two segments (L1 and L2). In the near future, the 500 mm isohyet does not change significantly under SSP126, contracts slightly under SSP245 and SSP585, and contracts significantly under SSP370. The central part of the 300 mm isohyet (located in the western part of R3) moves westwards under SSP126 and eastwards under SSP245, SSP370, and SSP585. In the far future, the 300 mm and 500 mm isohyets do not move significantly under SSP245 and SSP585. The 500 mm isohyet expands slightly under SSP126 and contracts significantly

under SSP370. The center of the 300 mm isohyet moves westwards under SSP126 and eastwards under SSP370.

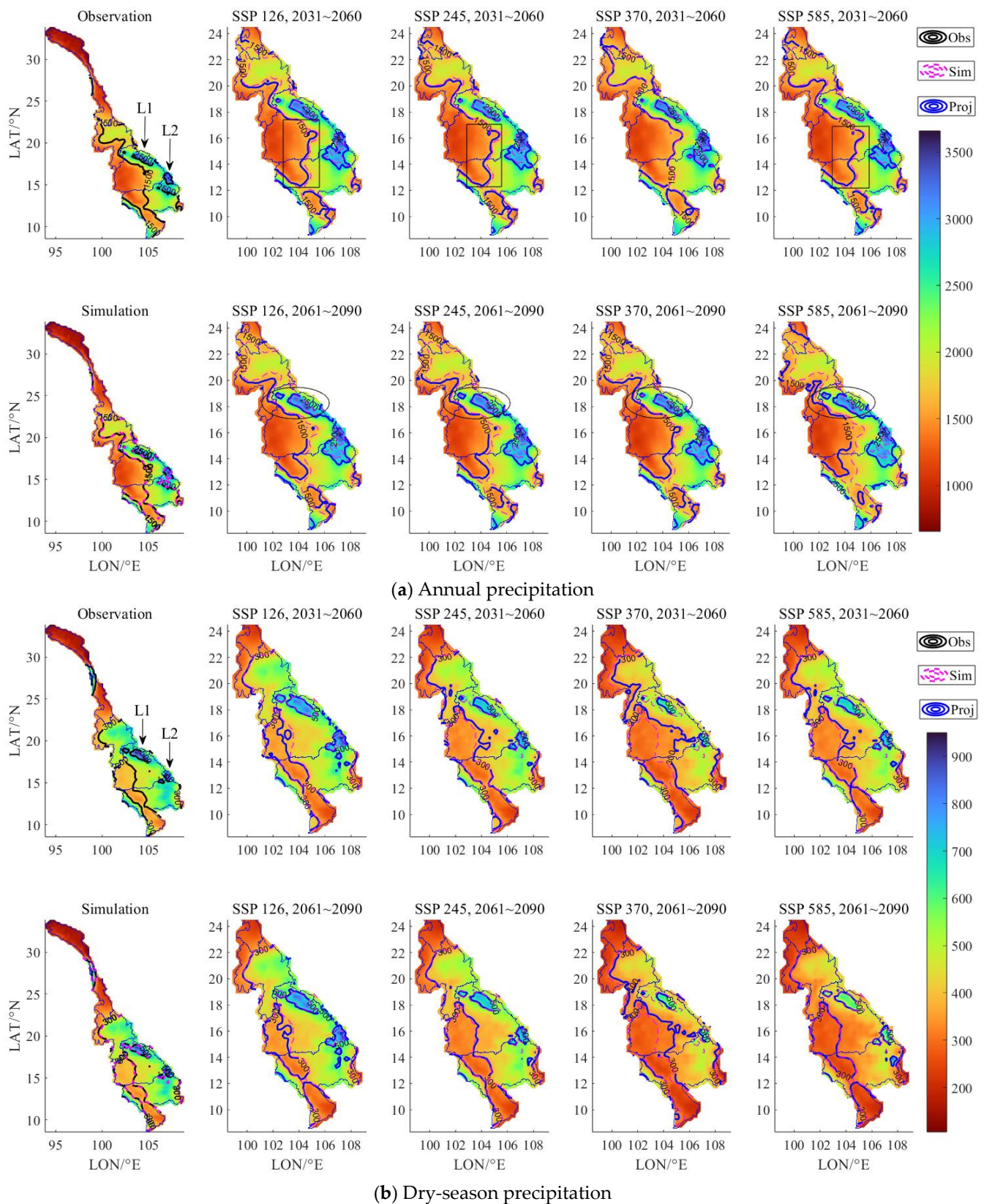


Figure 12. Changes in the spatial pattern of annual and dry-season precipitation under different scenarios in the future.

5. Discussion: Reliability of Future Projections

According to Section 4.1, there are still some biases in the climate simulations after bias treatment. Here, MS has been used to quantitatively assess the reliability of future projections. MS is calculated on the basis of the simulation of each model without observation, thus facilitating assessment of the reliability of future projections. According to the principle of MS, if the results of each model are more similar, the projection is considered more reliable [111]. To verify the rationality of the MS, we examined the spatio-temporal relationship between the RMSE (based on the multi-model ensemble) and the MS (based on the single model) in the historical period. Figure 13a,b show that the spatial distribution of RMSE and MS varies with good consistency on annual, monthly, and daily time scales. That is, MS is also higher in regions with higher RMSE and lower in regions with lower RMSE. Figure 13c shows the linear relationship between RMSE and MS, and the coefficients of determination on annual, monthly, and daily scales are 0.76, 0.8, and 0.64, respectively, indicating the existence of a good linear relationship between RMSE and MS. The above conclusions indicate that the MS results based on each model can show the performance of projections based on the MME.

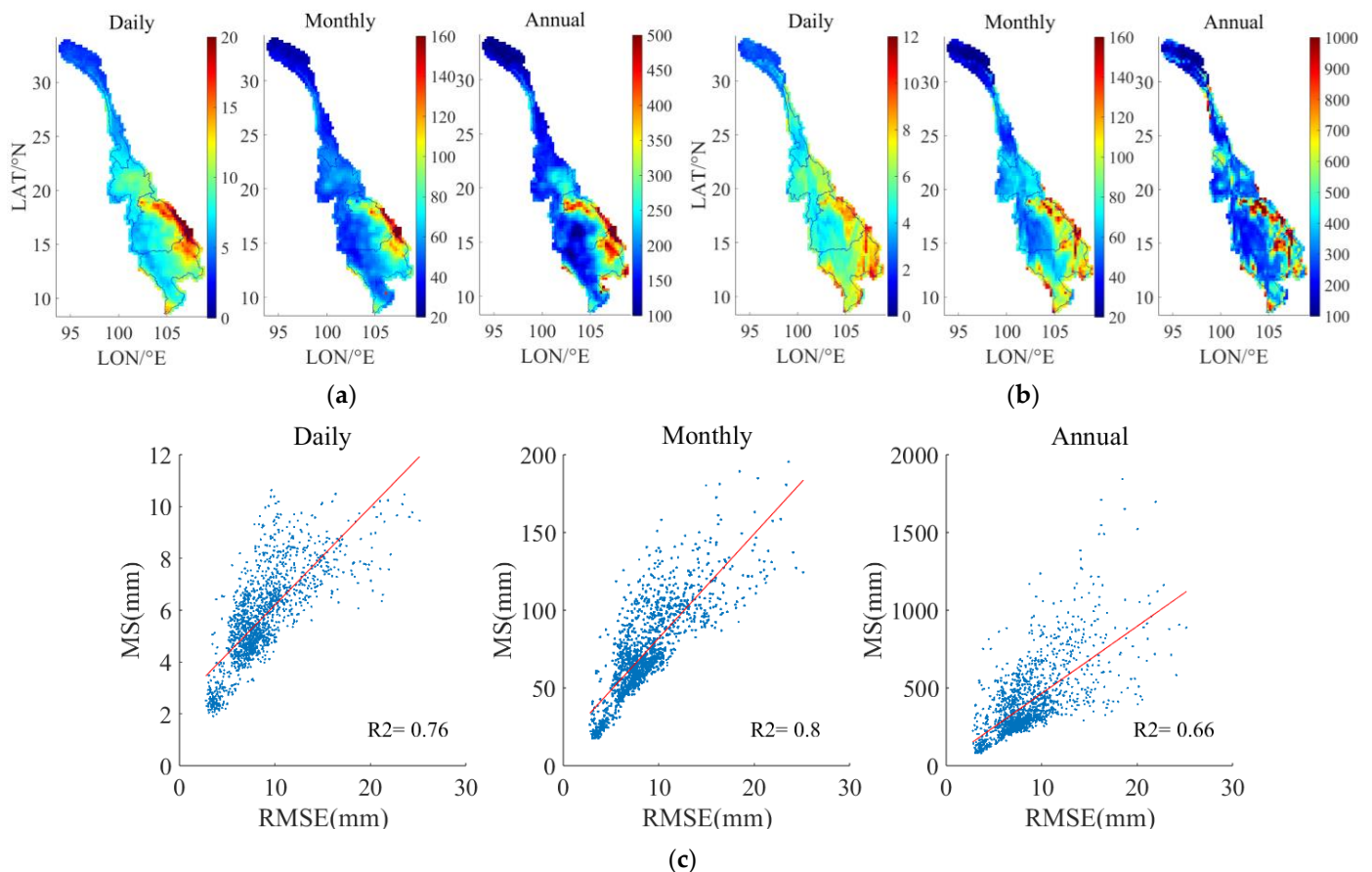


Figure 13. Spatial changes in RMSE and MS and their relationships at different time scales over the historical period. (a) RMSE. (b) MS. (c) Relationship between RMSE and MS (R^2 denotes the coefficient of determination).

It is important to note that we can qualitatively understand the relative reliability of future precipitation projections primarily through the spatial distribution of MS, and such information can suggest regions where we need to focus on improving climate models in the future. For example, during the historical period (on the same time scale), the MS results in the eastern parts of R3 and R4 were significantly higher than in other regions, indicating that the reliability of climate modelling in these regions was relatively lower.

than in other regions, and a similar conclusion can be drawn from the spatial distribution of RMSE.

Figure 14 shows the MS results for daily, monthly, and annual precipitation projections under each future scenario. The spatial distribution of MS between the scenarios is generally consistent and in line with the MS for the historical period (Figure 13b). The spatial distribution of MS at all time scales is also more consistent, being higher in eastern R3 and eastern and southern R4 than in other regions. This suggests that these regions have greater inter-model differences in precipitation projections than other regions, have relatively lower confidence in their future precipitation projections, and are priority regions for future improvements in climate models.

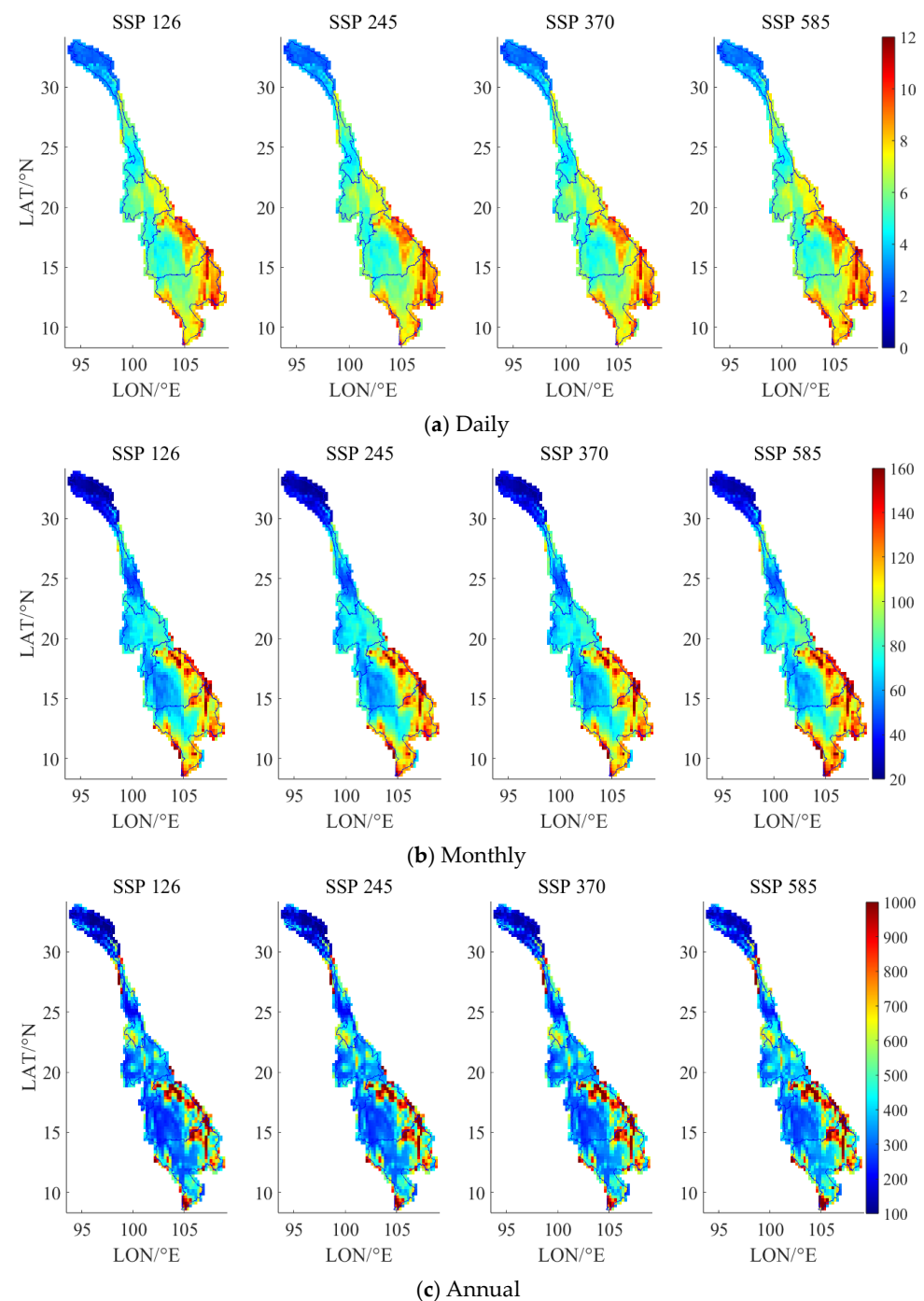


Figure 14. Spatial distribution of average MS at different time scales under future scenarios.

6. Conclusions

To gain insight into the characteristics of future precipitation in the LMRB, the CMIP6 daily precipitation data were used in this study. After assessing the simulation capabilities of climate models, bias correction, and multi-model ensemble, we obtained more reliable projections of future precipitation. Based on the spatial characteristics of precipitation, the LMRB was divided into four regions and two future periods (near future, 2031–2050, and far future, 2061–2090) were selected to analyze the changes in precipitation climatology, seasonal characteristics of precipitation, compositional structure of daily precipitation, and spatial distribution of precipitation.

In terms of precipitation climatology, future precipitation tends to increase in the whole basin and all sub-regions, with the lowest rate of increase under SSP126, a higher rate under SSP245 and SSP370, and the highest rate of increase under SSP585 (about twice as much as under SSP245 or SSP370). The rates of increase under SSP126, SSP245, and SSP370 are more evenly distributed across the basin, with most areas below 200 mm/100 a and localized rates of increase in the lower LRB and eastern lower and middle MRB (up to 500 mm/100 a) higher than in other areas. Under SSP585, the rates of increase in areas with annual precipitation above 2500 mm are all higher than 500 mm/100 a and even up to 800 mm/100 a. In the near future (2031–2060), the precipitation anomalies in the LMRB under the four SSP scenarios are 89 mm, 71 mm, 23 mm, and 70 mm, respectively, and in the far future (2061–2090) they are 136 mm, 142 mm, 114 mm, and 227 mm. In both the near and far futures, the anomalies are higher in the lower MRB and the Mekong Delta than in other regions, while they are lower in the middle MRB.

Spring and winter precipitation tended to increase in the north and decrease in the south, with spring precipitation in the Mekong Delta decreasing under all scenarios and winter precipitation in the central MRB (eastern Thailand and northern Laos) decreasing under SSP370 and SSP585. Summer and autumn precipitation showed a significant increasing trend (0.05 significance) for almost the whole basin, and the increase was greater with higher radiative forcing. For monthly precipitation in the wet season (May–October), there was a decrease in precipitation in May and an increase in each month from June to October, and the increase was greater in the far future than in the near future. The ratio of wet- to dry-season precipitation (R_{wd}) in the LMRB shows an increasing trend under all future scenarios, indicating an increase in the difference between wet- and dry-season precipitation in the future.

We classified daily precipitation into seven classes according to precipitation intensity and analyzed changes in the frequency of occurrence of daily precipitation of different intensities in the future. The results showed that changes in the compositional structure of daily precipitation occurred mainly in the far future. In the far future, under four SSP scenarios, the LRB is dominated by a 3–5% increase in the number of precipitation days with 5–10 mm/d and the MRB is dominated by a 3–5% increase in the number of precipitation days with 10–20 mm/d. The number of days with no precipitation (0–0.5 mm/d) mainly decreased in most parts of the basin under each scenario. The frequency of days with daily precipitation of 20–35 mm increased by about 3% in local areas of the middle and lower MRB, while the number of days with daily precipitation of more than 35 mm showed no significant change over the whole basin.

We chose the 2500 mm and 1500 mm isohyets as representative precipitation isohyets for annual precipitation. In the near future under the SSP126, SSP245, and SSP585 scenarios and in the far future under all four SSP scenarios, the 2500 mm isohyet extends outwards in a circular pattern and the center of the 1500 mm isohyet moves westwards; i.e., the area of annual precipitation exceeding both the 2500 mm and 1500 mm isohyets will expand. We also used the 300 mm and 500 mm isohyets as representative isohyets for dry-season precipitation and found that the 500 mm isohyet shrinks significantly towards the center of the ring under SSP370 (both in the near and far future). The 300 mm isohyet (in roughly the north–south direction) moves eastwards under SSP245, SSP370, and SSP585 in the near

future and under SSP370 in the far future; i.e., the area of dry-season precipitation below 300 mm has expanded.

In the future, the LMRB will become wetter on an annual scale, but on a seasonal scale there is a trend towards decreasing spring and winter precipitation in some areas. This, together with a future increase in R_{wd} , will further exacerbate the uneven intra-annual distribution of precipitation and water resources in the LMRB. On a daily scale, the occurrence of 10–20 mm/d of precipitation has increased in most areas, and the occurrence of 20–35 mm/d of precipitation has increased in the lower MRB, which may trigger more severe flooding in the lower MRB. The spatial and temporal mismatch between precipitation and irrigation water demand is a major challenge for agricultural development in the lower MRB. However, dry-season precipitation (a period of high irrigation demand) is expected to decrease further in the coming period, posing an even greater challenge to irrigated agriculture.

Author Contributions: Conceptualization, Z.S. and Y.L.; methodology, Z.S. and G.W.; data curation, Z.S. and J.J.; visualization, Z.S. and C.L.; writing—original draft, Z.S. and H.C.; review and funding acquisition, Y.L., J.Z. and L.T. All authors have read and agreed to the published version of the manuscript.

Funding: This research was supported by the National Key Research and Development Program of China (No. 2022YFC3201701) and the National Natural Science Foundation of China (52079079, U2240203, 52121006).

Data Availability Statement: The MSWEP gridded precipitation dataset and CMIP6 models' data are available online. MSWEP: <http://www.gloh2o.org/mswep/>, CMIP6 <https://esgfnode.llnl.gov/search/cmip6>, all accessed on 30 May 2023.

Conflicts of Interest: The authors declare no conflict of interest.

References

- Schneider, U.; Finger, P.; Meyer-Christoffer, A.; Rustemeier, E.; Ziese, M.; Becker, A. Evaluating the Hydrological Cycle over Land Using the Newly-Corrected Precipitation Climatology from the Global Precipitation Climatology Centre (GPCC). *Atmosphere* **2017**, *8*, 52. [CrossRef]
- Sun, Q.; Miao, C.; Duan, Q.; Ashouri, H.; Sorooshian, S.; Hsu, K.-L. A review of global precipitation data sets: Data sources, estimation, and intercomparisons. *Rev. Geophys.* **2018**, *56*, 79–107. [CrossRef]
- Stassen, C.; Dietmar, D.; Chadwick, R. Conceptual deconstruction of the simulated precipitation response to climate change. *Clim. Dynam.* **2020**, *55*, 613–630. [CrossRef]
- Stephens, G.L.; Hu, Y. Are climate-related changes to the character of global-mean precipitation predictable? *Environ. Res. Lett.* **2010**, *5*, 025209. [CrossRef]
- Papalexiou, S.M.; Montanari, A. Global and regional increase of precipitation extremes under global warming. *Water Resour. Res.* **2019**, *55*, 4901–4914. [CrossRef]
- Zhang, Y.; Wang, K. Global precipitation system scale increased from 2001 to 2020. *J. Hydrol.* **2023**, *616*, 128768. [CrossRef]
- Li, X.; Zhai, G.; Gao, S.; Shen, X. Decadal trends of global precipitation in the recent 30 years. *Atmos. Sci. Lett.* **2015**, *16*, 22–26. [CrossRef]
- Zhang, Y.; Wang, K. Global precipitation system size. *Environ. Res. Lett.* **2021**, *16*, 054005. [CrossRef]
- Contractor, S.; Donat, M.G.; Alexander, L.V. Changes in Observed Daily Precipitation over Global Land Areas since 1950. *J. Clim.* **2021**, *34*, 3–19. [CrossRef]
- Sun, Y.; Zhang, X.; Ding, Y.; Chen, D.; Qin, D.; Zhai, P. Understanding human influence on climate change in China. *Natl. Sci. Rev.* **2022**, *9*, nwab113. [CrossRef]
- Adler, R.F.; Sapiiano, M.R.P.; Huffman, G.J.; Wang, J.-J.; Gu, G.; Bolvin, D.; Chiu, L.; Schneider, U.; Becker, A.; Nelkin, E. The Global Precipitation Climatology Project (GPCP) Monthly Analysis (New Version 2.3) and a Review of 17 Global Precipitation. *Atmosphere* **2018**, *9*, 138. [CrossRef] [PubMed]
- O'gorman, P.A.; Allan, R.P.; Byrne, M.P.; Previdi, M. Energetic constraints on precipitation under climate change. *Surv. Geophys.* **2012**, *33*, 585–608. [CrossRef]
- Grassl, H. Climate change challenges. *Surv. Geophys.* **2011**, *32*, 319–328. [CrossRef]
- Hoegh-Guldberg, O.; Jacob, D.; Taylor, M.; Bolaños, T.G.; Bindi, M.; Brown, S.; Camilloni, I.A.; Diedhiou, A.; Djalante, R.; Ebi, K.; et al. The human imperative of stabilizing global climate change at 1.5 °C. *Science* **2019**, *365*, eaaw6974. [CrossRef]
- Li, Z.; Liu, T.; Huang, Y.; Peng, J.; Ling, Y. Evaluation of the CMIP6 precipitation simulations over global land. *Earths. Future* **2022**, *10*, e2021EF002500. [CrossRef]

16. Lau, W.K.-M.; Wu, H.-T.; Kim, K.-M. A canonical response of precipitation characteristics to global warming from CMIP5 models. *Geophys. Res. Lett.* **2013**, *40*, 3163–3169. [\[CrossRef\]](#)
17. Liu, Y.; Chen, J.; Pan, T.; Liu, Y.; Zhang, Y.; Ge, Q.; Ciais, P.; Penuelas, J. Global socioeconomic risk of precipitation extremes under climate change. *Earths. Future* **2020**, *8*, e2019EF001331. [\[CrossRef\]](#)
18. Zhang, W.; Zhou, T. Increasing impacts from extreme precipitation on population over China with global warming. *Sci. Bull.* **2020**, *65*, 243–252. [\[CrossRef\]](#)
19. Billi, P.; Fazzini, M. Global change and river flow in Italy. *Global Planet. Chang.* **2017**, *155*, 234–246. [\[CrossRef\]](#)
20. Murray, S.J.; Foster, P.N.; Prentice, I.C. Future global water resources with respect to climate change and water withdrawals as estimated by a dynamic global vegetation model. *J. Hydrol.* **2012**, *448–449*, 14–29. [\[CrossRef\]](#)
21. Calzadilla, A.; Rehdanz, K.; Betts, R.; Falloon, P.; Wiltshire, A.; Tol, R.S.J. Climate change impacts on global agriculture. *Clim. Chang.* **2013**, *120*, 357–374. [\[CrossRef\]](#)
22. Sloat, L.L.; Gerber, J.S.; Samberg, L.H.; Smith, W.K.; Herrero, M.; Ferreira, L.G.; Godde, C.M.; West, P.C. Increasing importance of precipitation variability on global livestock grazing lands. *Nat. Clim. Chang.* **2018**, *8*, 214–218. [\[CrossRef\]](#)
23. Murray-Tortarolo, G.N.; Jaramillo, V.J. Precipitation extremes in recent decades impact cattle populations at the global and national scales. *Sci. Total Environ.* **2020**, *736*, 139557. [\[CrossRef\]](#)
24. Su, J.; Zhao, Y.; Bai, Y. Asymmetric responses of leaf litter decomposition to precipitation changes in global terrestrial ecosystem. *J. Clean. Prod.* **2023**, *387*, 135898. [\[CrossRef\]](#)
25. Gherardi, L.A.; Sala, O.E. Effect of interannual precipitation variability on dryland productivity: A global synthesis. *Glob. Chang. Biol.* **2019**, *25*, 269–276. [\[CrossRef\]](#)
26. Cheng, Q.; Liu, P.; Xia, J.; Ming, B.; Cheng, L.; Chen, J.; Xie, K.; Liu, Z.; Li, X. Contribution of complementary operation in adapting to climate change impacts on a large-scale wind–solar–hydro system: A case study in the Yalong River Basin, China. *Appl. Energy* **2022**, *325*, 119809. [\[CrossRef\]](#)
27. Hamududu, B.; Killingtveit, A. Assessing Climate Change Impacts on Global Hydropower. *Energies* **2012**, *5*, 305–322. [\[CrossRef\]](#)
28. Engeland, K.; Borga, M.; Creutin, J.-D.; François, B.; Ramos, M.-H.; Vidal, J.-P. Space-time variability of climate variables and intermittent renewable electricity production—A review. *Renew. Sust. Energ. Rev.* **2017**, *79*, 600–617. [\[CrossRef\]](#)
29. Gobiet, A.; Kotlarski, S.; Beniston, M.; Heinrich, G.; Rajczak, J.; Stoffel, M. 21st century climate change in the European Alps—A review. *Sci. Total Environ.* **2014**, *493*, 1138–1151. [\[CrossRef\]](#)
30. Zhao, D.; Zhang, L.; Zhou, T. Detectable anthropogenic forcing on the long-term changes of summer precipitation over the Tibetan Plateau. *Clim. Dyn.* **2022**, *59*, 1939–1952. [\[CrossRef\]](#)
31. Xie, Z.; Huete, A.; Cleverly, J.; Phinn, S.; McDonald-Madden, E.; Cao, Y.; Qin, F. Multi-climate mode interactions drive hydrological and vegetation responses to hydroclimatic extremes in Australia. *Remote Sens. Environ.* **2019**, *231*, 111270. [\[CrossRef\]](#)
32. Qian, T.; Dai, A.; Trenberth, K.E. Hydroclimatic Trends in the Mississippi River Basin from 1948 to 2004. *J. Clim.* **2007**, *20*, 4599–4614. [\[CrossRef\]](#)
33. Le, J.A.; El-Askary, H.M.; Allali, M.; Sayed, E.; Sweliem, H.; Piechota, T.C.; Struppa, D.C. Characterizing El Niño-Southern Oscillation Effects on the Blue Nile Yield and the Nile River Basin Precipitation using Empirical Mode Decomposition. *Earth Syst. Environ.* **2020**, *4*, 699–711. [\[CrossRef\]](#)
34. Yin, X.; Gruber, A. Validation of the abrupt change in GPCP precipitation in the Congo River Basin. *Int. J. Climatol.* **2010**, *30*, 110–119. [\[CrossRef\]](#)
35. Haghtalab, N.; Moore, N.; Heerspink, B.P.; Hyndman, D.W. Evaluating spatial patterns in precipitation trends across the Amazon basin driven by land cover and global scale forcings. *Theor. Appl. Climatol.* **2020**, *140*, 411–427. [\[CrossRef\]](#)
36. Hu, Z.; Zhou, Q.; Chen, X.; Qian, C.; Wang, S.; Li, J. Variations and changes of annual precipitation in Central Asia over the last century. *Int. J. Climatol.* **2017**, *37*, 157–170. [\[CrossRef\]](#)
37. Chen, F.; Huang, W.; Jin, L.; Chen, J.; Wang, J. Spatiotemporal precipitation variations in the arid Central Asia in the context of global warming. *Sci. China Earth Sci.* **2011**, *54*, 1812–1821. [\[CrossRef\]](#)
38. Irannezhad, M.; Liu, J.; Chen, D. Influential climate teleconnections for spatiotemporal precipitation variability in the Lancang-Mekong River basin from 1952 to 2015. *J. Geophys. Res-Atmos.* **2020**, *125*, e2020JD033331. [\[CrossRef\]](#)
39. Zhang, Q.; Peng, J.; Xu, C.Y.; Singh, V.P. Spatiotemporal variations of precipitation regimes across Yangtze River Basin, China. *Theor. Appl. Climatol.* **2014**, *115*, 703–712. [\[CrossRef\]](#)
40. Xu, K.; Milliman, J.D.; Xu, H. Temporal trend of precipitation and runoff in major Chinese Rivers since 1951. *Global Planet. Chang.* **2010**, *73*, 219–232. [\[CrossRef\]](#)
41. Li, Q.; Zeng, T.; Chen, Q.; Han, X.; Weng, X.; He, P.; Zhou, Z.; Du, Y. Spatio-temporal changes in daily extreme precipitation for the Lancang-Mekong River Basin. *Nat. Hazards* **2023**, *115*, 641–672. [\[CrossRef\]](#)
42. Liu, J.; Chen, D.; Mao, G.; Irannezhad, M.; Pokhrel, Y. Past and Future Changes in Climate and Water Resources in the Lancang-Mekong River Basin: Current Understanding and Future Research Directions. *Engineering* **2022**, *13*, 144–152. [\[CrossRef\]](#)
43. Yao, T.; Bolch, T.; Chen, D.; Gao, J.; Immerzeel, W.; Piao, S.; Su, F.; Thompson, L.; Wada, Y.; Wang, L.; et al. The imbalance of the Asian water tower. *Nat. Rev. Earth Environ.* **2022**, *3*, 618–632. [\[CrossRef\]](#)
44. Zhao, Y.; Zhou, T.J.; Zhang, W.X.; Li, J. Change in precipitation over the Tibetan Plateau projected by weighted CMIP6 models. *Adv. Atmos. Sci.* **2022**, *39*, 1133–1150. [\[CrossRef\]](#)

45. Lu, H.-L.; Li, F.-F.; Gong, T.-L.; Gao, Y.-H.; Li, J.-F.; Qiu, J. Reasons behind seasonal and monthly precipitation variability in the Qinghai-Tibet Plateau and its surrounding areas during 1979~2017. *J. Hydrol.* **2023**, *619*, 129329. [[CrossRef](#)]
46. Chen, R.; Duan, K.; Shang, W.; Shi, P.; Meng, Y.; Zhang, Z. Increase in seasonal precipitation over the Tibetan Plateau in the 21st century projected using CMIP6 models. *Atmos. Res.* **2022**, *277*, 106306. [[CrossRef](#)]
47. Zhong, R.; Zhao, T.; He, Y.; Chen, X. Hydropower change of the water tower of Asia in 21st century: A case of the Lancang River hydropower base, upper Mekong. *Energy* **2019**, *179*, 685–696. [[CrossRef](#)]
48. Zhong, S.; Zhu, Y.; Zhao, J.; Shen, L. A Collaborative Framework for Hydropower Development and Sustainable Livelihood of Farmers in the Lancang-Mekong River Basin: A Review with the Perspective of Energy-Water-Food Nexus. *Water* **2022**, *14*, 499. [[CrossRef](#)]
49. Fan, X.; Luo, X. Precipitation and Flow Variations in the Lancang–Mekong River Basin and the Implications of Monsoon Fluctuation and Regional Topography. *Water* **2019**, *11*, 2086. [[CrossRef](#)]
50. Wang, W.; Lu, H.; Leung, L.R.; Li, H.-Y.; Zhao, J.; Tian, F.; Yang, K.; Sothea, K. Dam construction in Lancang-Mekong River Basin could mitigate future flood risk from warming-induced intensified rainfall. *Geophys. Res. Lett.* **2017**, *44*, 10378–10386. [[CrossRef](#)]
51. Jing, W.; Zhao, X.; Yao, L.; Jiang, H.; Xu, J.; Yang, J.; Li, Y. Variations in terrestrial water storage in the Lancang-Mekong river basin from GRACE solutions and land surface model. *J. Hydrol.* **2020**, *580*, 124258. [[CrossRef](#)]
52. Gao, J.; Castelletti, A.; Burlado, P.; Wang, H.; Zhao, J. Soft-cooperation via data sharing eases transboundary conflicts in the Lancang-Mekong River Basin. *J. Hydrol.* **2022**, *606*, 12746. [[CrossRef](#)]
53. Gao, J.; Zhao, J.; ASCE, M.; Wang, H. Dam-Impacted Water–Energy–Food Nexus in Lancang-Mekong River Basin. *J. Water Res. Pl-ASCE* **2021**, *147*, 04021010. [[CrossRef](#)]
54. Do, P.; Tian, F.; Zhu, T.; Zohidov, B.; Ni, G.; Lu, H.; Liu, H. Exploring synergies in the water-food-energy nexus by using an integrated hydro-economic optimization model for the Lancang-Mekong River basin. *Sci. Total Environ.* **2020**, *728*, 137996. [[CrossRef](#)] [[PubMed](#)]
55. Kayiranga, A.; Chen, B.; Guo, L.; Measho, S.; Hirwa, H.; Liu, S.; Bofana, J.; Sun, S.; Wang, F.; Karamage, F.; et al. Spatiotemporal variations of forest ecohydrological characteristics in the Lancang-Mekong region during 1992-2016 and 2020-2099 under different climate scenarios. *Agr. Forest Meteorol.* **2021**, *310*, 108662. [[CrossRef](#)]
56. Mekong River Commission 2010. *State of the Basin Report 2010*; Mekong River Commission: Vientiane, Laos, 2010.
57. Lu, Y.; Tian, F.; Guo, L.; Borzi, I.; Patil, R.; Wei, J.; Liu, D.; Wei, Y.; Yu, D.J.; Sivapalan, M. Socio-hydrologic modeling of the dynamics of cooperation in the transboundary Lancang–Mekong River. *Hydrol. Earth Syst. Sci.* **2021**, *25*, 1883–1903. [[CrossRef](#)]
58. Feng, Y.; Wang, W.; Suman, D.; Yu, S.; He, D. Water Cooperation Priorities in the Lancang-Mekong River Basin Based on Cooperative Events Since the Mekong River Commission Establishment. *Chinese Geogr. Sci.* **2019**, *29*, 58–69. [[CrossRef](#)]
59. Wei, J.; Wei, Y.; Tian, F.; Nott, N.; Wit, C.; Guo, L.; Lu, Y. News media coverage of conflict and cooperation dynamics of water events in the Lancang–Mekong River basin. *Hydrol. Earth Syst. Sci.* **2021**, *25*, 1603–1615. [[CrossRef](#)]
60. Tang, J.; Cao, H. Drought and flood occurrences in the Lancang River Basin during the last 60 years: Their variations and teleconnections with monsoons. *J. Water Clim. Chang.* **2020**, *11*, 1798–1810. [[CrossRef](#)]
61. Liu, Z.; Wang, R.; Yao, Z. Climate change and its impact on water availability of large international rivers over the mainland Southeast Asia. *Hydrol. Process.* **2018**, *32*, 3966–3977. [[CrossRef](#)]
62. Palanisamy, B.; Narasimhan, B.; Paul, S.; Srinivasan, R.; Wangpimool, W.; Sith, R.; Sayasane, R. Development and propagation of hydrologic drought from meteorological and agricultural drought in the Mekong River Basin. *Hydrol. Process.* **2023**, *37*, e14935. [[CrossRef](#)]
63. Delgado, J.M.; Merz, B.; Apel, H. A climate-flood link for the lower Mekong River. *Hydrol. Earth Syst. Sci.* **2012**, *16*, 1533–1541. [[CrossRef](#)]
64. Irannezhad, M.; Liu, J.; Chen, D. Extreme precipitation variability across the Lancang-Mekong River Basin during 1952–2015 in relation to teleconnections and summer monsoons. *Int. J. Climatol.* **2022**, *42*, 2614–2638. [[CrossRef](#)]
65. Guo, Y.; Yang, X.; Chen, X.; Mei, Y.; Di, C. Air temperature and precipitation variation trends of the Lancang river upstream from 1957 to 2011. *Therm. Sci.* **2013**, *17*, 1383–1388. [[CrossRef](#)]
66. Wang, X.; Cui, G.; Wu, F.; Li, C. Analysis of temporal-spatial precipitation variations during the crop growth period in the Lancang River basin, southwestern China. *Ecol. Eng.* **2015**, *76*, 47–56. [[CrossRef](#)]
67. Hapuarachchi, H.A.P.; Takeuchi, K.; Zhou, M.; Kiem, A.S.; Georgievski, M.; Magome, J.; Ishidaira, H. Investigation of the Mekong River basin hydrology for 1980–2000 using the YHyM. *Hydrol. Process.* **2008**, *22*, 1246–1256. [[CrossRef](#)]
68. Mondal, A.; Le, M.-H.; Lakshmi, V. Land use, climate, and water change in the Vietnamese Mekong Delta (VMD) using earth observation and hydrological modeling. *J. Hydrol-Reg. Stud.* **2022**, *42*, 101132. [[CrossRef](#)]
69. Try, S.; Tanaka, S.; Tanaka, K.; Sayama, T.; Khujanazarov, T.; Oeurng, C. Comparison of CMIP5 and CMIP6 GCM performance for flood projections in the Mekong River Basin. *J. Hydrol-Reg. Stud.* **2022**, *40*, 101035. [[CrossRef](#)]
70. Anh, T.D.; Hoang, P.L.; Bui, D.M.; Rutschmann, P. Modelling seasonal flows alteration in the Vietnamese Mekong Delta under upstream discharge changes, rainfall changes and sea level rise. *Int. J. River Basin Ma.* **2019**, *17*, 435–449. [[CrossRef](#)]
71. Cook, B.I.; Bell, A.R.; Anchukaitis, K.J.; Buckley, B.M. Snow cover and precipitation impacts on dry season streamflow in the Lower Mekong Basin. *J. Geophys. Res.* **2012**, *117*, D16116. [[CrossRef](#)]
72. Try, S.; Tanaka, S.; Tanaka, K.; Sayama, T.; Lee, G.; Oeurng, C. Assessing the effects of climate change on flood inundation in the lower Mekong Basin using high-resolution AGCM outputs. *Prog. Earth Planet. Sci.* **2020**, *7*, 34. [[CrossRef](#)]

73. Sun, C.; Xiao, Z.-N.; Nguyen, M. Projection on precipitation frequency of different intensities and precipitation amount in the Lancang-Mekong River basin in the 21st century. *Adv. Clim. Chang. Res.* **2021**, *12*, 162–171. [\[CrossRef\]](#)
74. Wang, S.; Zhang, L.; She, D.; Wang, G.; Zhang, Q. Future projections of flooding characteristics in the Lancang-Mekong river basin under climate change. *J. Hydrol.* **2021**, *602*, 126778. [\[CrossRef\]](#)
75. Li, Y.; Lu, H.; Yang, K.; Wang, W.; Tang, Q.; Khem, S.; Huang, Y. Meteorological and hydrological droughts in Mekong river basin and surrounding areas under climate change. *J. Hydrol.* **2021**, *36*, 100873. [\[CrossRef\]](#)
76. Sun, C.; Xiao, Z.; Sun, J.; Yu, E. Projection of temperature change and extreme temperature events in the Lancang-Mekong River basin. *Atmos. Ocean. Sci. Lett.* **2020**, *13*, 16–25. [\[CrossRef\]](#)
77. Ruiz-Barradas, A.; Nigam, S. Hydroclimate variability and change over the Mekong river basin: Modeling and predictability and policy implications. *J. Hydrometeorol.* **2018**, *19*, 849–869. [\[CrossRef\]](#)
78. Huang, Y.; Wang, F.; Li, Y.; Cai, T. Multi-model ensemble simulation and projection in the climate change in the Mekong river basin. Part I: Temperature. *Environ. Monit. Assess.* **2014**, *186*, 7513–7523. [\[CrossRef\]](#)
79. Iqbal, Z.; Shahid, S.; Ahmed, K.; Ismail, T.; Ziarh, G.F.; Chung, E.; Wang, X. Evaluation of CMIP6 GCM rainfall in mainland Southeast Asia. *Atmos. Res.* **2021**, *254*, 105525. [\[CrossRef\]](#)
80. Zhu, Y.; Yang, S. Evaluation of CMIP6 for historical temperature and precipitation over the Tibetan Plateau and its comparison with CMIP5. *Adv. Clim. Chang. Res.* **2020**, *11*, 239–251. [\[CrossRef\]](#)
81. Lun, Y.; Liu, L.; Cheng, L.; Li, X.; Li, H.; Xu, Z. Assessment of GCMs simulation performance for precipitation and temperature from CMIP5 to CMIP6 over the Tibetan Plateau. *Int. J. Climatol.* **2021**, *41*, 3994–4018. [\[CrossRef\]](#)
82. Beck, H.E.; Wood, E.F.; Pan, M.; Fisher, C.K.; Miralles, D.G.; Dijk, A.I.J.M.; McVicar, T.R.; Adler, R.F. MSWEP V2 global 3-hourly 0.1° precipitation: Methodology and quantitative assessment. *Bull. Am. Meteorol. Soc.* **2019**, *100*, 473–500. [\[CrossRef\]](#)
83. Beck, H.E.; Dijk, A.I.J.M.; Levizzani, V.; Schellekens, J.; Miralles, D.G.; Martens, B.; Roo, A.D. MSWEP: 3-hourly 0.25° global gridded precipitation (1979–2015) by merging gauge, satellite, and reanalysis data. *Hydrol. Earth Syst. Sci.* **2017**, *21*, 589–615. [\[CrossRef\]](#)
84. Beck, H.E.; Vergopolan, N.; Pan, M.; Levizzani, V.; Dijk, A.I.J.M.V.; Weedon, G.P.; Brocca, L.; Pappenberger, F.; Huffman, G.J.; Wood, E.F. Global-scale evaluation of 22 precipitation datasets using gauge observations and hydrological modeling. *Hydrol. Earth Syst. Sci.* **2017**, *21*, 6201–6217. [\[CrossRef\]](#)
85. Liu, J.; Shangguan, D.; Liu, S.; Ding, Y.; Wang, S.; Wang, X. Evaluation and comparison of CHIRPS and MSWEP daily-precipitation products in the Qinghai-Tibet Plateau during the period of 1981–2015. *Atmos. Res.* **2019**, *230*, 104634. [\[CrossRef\]](#)
86. Li, L.; Wang, Y.; Wang, L.; Hu, Q.; Zhu, Z.; Li, L.; Li, C. Spatio-temporal accuracy evaluation of MSWEP daily precipitation over the Huaihe River Basin, China: A comparison study with representative satellite- and reanalysis-based products. *J. Geogr. Sci.* **2022**, *32*, 2271–2290. [\[CrossRef\]](#)
87. Prakash, S. Performance assessment of CHIRPS, MSWEP, SM2RAIN-CCI, and TMPA precipitation products across India. *J. Hydrol.* **2019**, *571*, 50–59. [\[CrossRef\]](#)
88. Ali, S.; Chen, Y.; Azmat, M.; Patient, M.K.; Ahmed, Z.; Richard, M.; Tariq, A. Long-term performance evaluation of the latest multi-source weighted-ensemble precipitation (MSWEP) over the highlands of Indo-Pak (1981–2009). *Remote Sens.* **2022**, *14*, 4773. [\[CrossRef\]](#)
89. Tang, X.; Zhang, J.; Wang, G.; Ruben, G.B.; Bao, Z.; Liu, Y.; Liu, C.; Jin, J. Error Correction of Multi-Source Weighted-Ensemble Precipitation (MSWEP) over the Lancang-Mekong River Basin. *Remote Sens.* **2021**, *13*, 312. [\[CrossRef\]](#)
90. Tang, X.; Zhang, J.; Gao, C.; Ruben, G.; Wang, G. Assessing the Uncertainties of Four Precipitation Products for SWAT Modeling in Mekong River Basin. *Remote Sens.* **2019**, *11*, 304. [\[CrossRef\]](#)
91. Tian, W.; Liu, X.; Wang, K.; Bai, P.; Liang, K.; Liu, C. Evaluation of six precipitation products in the Mekong River Basin. *Atmos. Res.* **2021**, *255*, 105539. [\[CrossRef\]](#)
92. Chen, J.; Brissette, F.P.; Chaumont, D.; Braun, M. Performance and uncertainty evaluation of empirical downscaling methods in quantifying the climate change impacts on hydrology over two North American River Basins. *J. Hydrol.* **2013**, *479*, 200–214. [\[CrossRef\]](#)
93. Yin, J.; Guo, S.; He, S.; Guo, J.; Hong, X.; Liu, Z. A copula-based analysis of projected climate changes to bivariate flood quantiles. *J. Hydrol.* **2018**, *566*, 23–42. [\[CrossRef\]](#)
94. Duan, Q.; Ajami, N.K.; Gao, X.; Sorooshian, S. Multi-model ensemble hydrologic prediction using Bayesian model averaging. *Adv. Water Res.* **2007**, *30*, 1371–1386. [\[CrossRef\]](#)
95. Wei, L.; Jiang, S.; Dong, J.; Ren, L.; Liu, Y.; Zhang, L.; Wang, M.; Duan, Z. Fusion of gauge-based, reanalysis, and satellite precipitation products using Bayesian model averaging approach: Determination of the influence of different input sources. *J. Hydrol.* **2023**, *618*, 129234. [\[CrossRef\]](#)
96. Raftery, A.E.; Gneiting, T.; Balabdaoui, F.; Polakowski, M. Using Bayesian model averaging to calibrate forecast ensembles. *Mon. Wea. Rev.* **2005**, *113*, 1155–1174. [\[CrossRef\]](#)
97. Sloughter, J.M.L.; Raftery, A.E.; Gneiting, T.; Fraley, C. Probabilistic quantitative precipitation forecasting using Bayesian model averaging. *Mon. Wea. Rev.* **2007**, *135*, 3209–3220. [\[CrossRef\]](#)
98. Kendall, M.; Gibbons, J.D. *Rank Correlation Methods*, 5th ed.; Edward Arnold: London, UK, 1990.
99. Mann, H.D. Nonparametric tests against trend. *Econom. J. Econom. Soc.* **1945**, *13*, 245–259. [\[CrossRef\]](#)

100. Moraglia, G.; Brattich, E.; Carbone, G. Precipitation trends in North and South Carolina, USA. *J. Hydrol-Reg. Stud.* **2022**, *44*, 101201. [[CrossRef](#)]
101. Ullah, S.; You, Q.; Zhang, Y.; Bhatti, A.S.; Ullah, W.; Hagan, D.F.T.; Ali, A.; Ali, G.; Jan, M.A.; Khan, S.N.; et al. Evaluation of CMIP5 models and projected changes in temperatures over South Asia under global warming of 1.5 °C, 2 °C, and 3 °C. *Atmos. Res.* **2020**, *246*, 105122. [[CrossRef](#)]
102. Pimonsree, S.; Kamworapan, S.; Gheewala, S.H.; Thongbhakdi, A.; Prueksakorn, K. Evaluation of CMIP6 GCMs performance to simulate precipitation over Southeast Asia. *Atmos. Res.* **2023**, *282*, 106522. [[CrossRef](#)]
103. Kuenzer, C.; Guo, H.; Huth, J.; Leinenkugel, P.; Li, X.; Dech, S. Flood mapping and flood dynamics of the mekong delta: ENVISAT-ASAR-WSM based time series analyses. *Remote Sens.* **2013**, *5*, 687–715. [[CrossRef](#)]
104. Raesaenen, T.A.; Kummu, M. Spatiotemporal influences of ENSO on precipitation and flood pulse in the mekong river basin. *J. Hydrol.* **2013**, *476*, 154–168. [[CrossRef](#)]
105. Try, S.; Tanaka, S.; Tanaka, K.; Sayama, T.; Hu, M.; Sok, T.; Oeurng, C. Projection of extreme flood inundation in the mekong river basin under 4K increasing scenario using large ensemble climate data. *Hydrol. Process.* **2020**, *34*, 4350–4364. [[CrossRef](#)]
106. Liu, J.; Wu, D.Y.; Li, Y.; Ren, H.; Zhao, Y.; Sun, X.; Zhang, H.; Ji, M. Spatiotemporal variation of precipitation on a global scale from 1960 to 2016 in a new normalized daily precipitation dataset. *Int. J. Climatol.* **2022**, *42*, 3648–3665. [[CrossRef](#)]
107. Guan, T.; Liu, Y.; Sun, Z.; Zhang, J.; Chen, H.; Wang, G.; Jin, J.; Bao, Z.; Qi, W. A Framework to Identify the Uncertainty and Credibility of GCMs for Projected Future Precipitation: A Case Study in the Yellow River Basin, China. *Front. Environ. Sci.* **2022**, *10*, 863575. [[CrossRef](#)]
108. Zeng, H.; Li, L.; Hu, J.; Liang, L.; Li, J.; Li, B.; Zhang, K. Accuracy validation of TRMM Multisatellite Precipitation Analysis daily precipitation products in the Lancang River Basin of China. *Theor. Appl. Climatol.* **2013**, *112*, 389–401. [[CrossRef](#)]
109. Wu, S.; Lei, Y. Multiscale Flood Disaster Risk Assessment in the Lancang-Mekong River Basin: A Focus on Watershed and Community Levels. *Atmosphere* **2023**, *14*, 657. [[CrossRef](#)]
110. Mekong River Commission. *Assessment of Basin-Wide Development Scenarios-Main Report*; Mekong River Commission: Vientiane, Laos, 2011.
111. Sun, Z.; Liu, Y.; Zhang, J.; Chen, H.; Shu, Z.; Guan, T.; Wang, G.; Jin, J.; Bao, Z.; Liu, C. Deterministic and probabilistic projections and their credibility in analyzing future precipitation variations in the Yellow River Basin, China. *J. Water Clim. Chang.* **2022**, *13*, 1806–1829. [[CrossRef](#)]

Disclaimer/Publisher's Note: The statements, opinions and data contained in all publications are solely those of the individual author(s) and contributor(s) and not of MDPI and/or the editor(s). MDPI and/or the editor(s) disclaim responsibility for any injury to people or property resulting from any ideas, methods, instructions or products referred to in the content.